Investigations of Few Layer MOFs and Anion Substituted Chromium (III) oxide

A thesis submitted
in partial fulfilment for the degree of

Master of Science

as a part of the

M. S. – Ph. D. Programme
(Chemistry)

by

Monali Moirangthem

New Chemistry Unit
Jawaharlal Nehru Centre for Advanced Scientific Research
(A Deemed University)
Bangalore, India

April 2014

Dedicated

to

My Family

DECLARATION

I hereby declare that the matter embodied in the thesis entitled "**Investigations of few layer MOFs and anion substituted Chromium (III) oxide**" is the result of investigation carried out by me under the supervision of Prof. C. N. R. Rao, FRS at the New Chemistry Unit, Jawaharlal Nehru Centre for Advanced Scientific Research, Bangalore, India and that it has not been submitted elsewhere for the award of nay degree or diploma.

In keeping with the general practice in reporting the scientific observations, due acknowledgement has been made whenever the work described is based on the findings of other investigators. Any omission that might have occurred due to oversight or error in judgement is regretted.

Bangalore ----------

Date: 4th April 2014 (Monali Moirangthem)

CERTIFICATE

I hereby certify that the work described in this thesis entitled "**Investigations of few layer MOFs and anion substituted Chromium (III) oxide**" has been carried out by Ms. Monali Moirangthem under my supervision at the New Chemistry Unit, Jawaharlal Nehru Centre for Advanced Scientific Research, Bangalore, India and that it has not been submitted elsewhere for the award of nay degree or diploma.

Bangalore — Prof. C. N. R. Rao

Date : 4th April 2014 — (Research Supervisor)

ACKNOWLEDGEMENT

It is with immense gratitude that I acknowledge the constant support and invaluable guidance of my research supervisor Prof. C. N. R. Rao, FRS. He introduced me to the field of Material Science and gave me the opportunity to work in the intriguing field of Magnetism. It has been truly an enriching experience to work under his supervision. His everlasting enthusiasm and his dedication towards science is my greatest source of inspiration.

I thank my collaborator Prof. R. Murugavel, Indian Institute of Bombay for providing me with the samples for magnetic and optical studies of few layers metal-organic frameworks.

I would like to take this opportunity to thank Dr. A. Govindaraj who had helped me in getting the essentials of my research work.

I am extremely thankful to Dr. B.E. Prasad and Mr. Rana Saha with whom I had worked on different research problems. Without their support and valuable suggestions, it would not have been possible for my work to be compiled into a thesis. I am indebted especially to Mr. Rana Saha for his encouraging advices and his undying support throughout my MS project.

I am grateful to all my lab mates Dr. Ramakrishna Matte, Nitesh, Urmimala, Rana, Moses, Lingampalli, Gopal, Pramoda, Ram, Sunita, Uttam, Sreedhar, Manoj, Anand, Dr. Prasad, Dr. Chithaiah, Dr. Vasu and Dr. Naidu for their help at various occasions whenever I had needed. I would like to thank Dr. Jayaramulu too for helping me in understanding MOF systems. I am thankful to Dr. Narendra and Ajmala for their guidance in the initial days when I did not have any knowledge of research.

I would like to express my sincere thanks to Prof. S. Balasubramanian, Prof. G. U. Kulkarni, Prof. S. M. Shivaprasad, Prof. A. Sundaresan, Prof. H. Ila, Prof. Aloknath Chakrabarti, Dr. Eswaramoorthy, Dr. T. K. Maji, Dr. Subi J. George, Dr. T. Govindaraju, Dr. Sebastian C. Peter, Dr. Sridhar Rajaram, Dr. Ranjan Datta, Dr. Ranjani Viswanatha

and Dr. Ujjal Gautam for their excellent courses. I would like to thank Prof. S. N. Bhat, Co-ordinator, POCE for the wonderful interactions.

I would like to thank the technical staffs of JNCASR specially Mr. Vasu, Mr. Anil, Mrs. Selvi Rajan, Mr. Mahesh, Mr. Jagdish and Mr. Shivaprasad for their help with the characterization of my samples.

I would like to thank JNCASR for funding my research work and providing the necessary research facilities.

I will be ever thankful to my teachers (school and college). I owe them for everything I am today.

I thank all my dearest friends Komal, Suseela, Debopreeti, Pallabi, Krishnendu, Mohini, Neelima, Dipanwita, Raaghesh and Sonu. My three years of stay in JNCASR has been so much fun-filled with countless memories in the company of you all. I would like to thank Sneha and her family for their support whenever I needed. I would like to thank all my friends specially Gaurav and Krishna who had helped me in getting access to many publications at various occasions.

I am blessed to have Hitesh as my friend. It is my pleasure to thank him for being by my side through thick and thin.

I take this opportunity to thank my cousins Che Esther and Da Bidyanand for their love and care.

Lastly, I would like to thank my family for their constant encouragement, love and affection.

I thank Lord for His blessings.

PREFACE

The thesis consists of three chapters presenting the results of investigation of few layer metal organic frameworks and anion substituted chromium (III) oxide.

Chapter 1 discusses the exfoliation of layered metal organic frameworks into few layer sheets. The investigation on magnetic and optical properties of the few layer nanosheets is presented.

Chapter 2 gives a brief introduction to magnetism and different types of magnetic materials. A brief discussion on exchange bias effect is also presented.

Chapter 3 discusses the substitution of nitrogen and fluorine in Chromium (III) oxide and its effects on the magnetic properties. Optical properties of the anion substituted Cr_2O_3 are also discussed.

CONTENTS

CHAPTER 1

Investigations of Few Layer Metal-Organic Frameworks

Abstract*:

Layered metal-organic frameworks *viz.*$[(C_{10}H_{13}O_3P)Co(H_2O)]$, $[Cu(C_8H_{10}O_3P)_2]_n$, $[Cu_6(H_2L)_3(H_2O)_{10}]_n.4H_2O$, $[(C_{10}H_{13}O_3P)Ni(H_2O)]$, $[(C_{10}H_{13}O_3P)Cu(H_2O)]$ and $[Cu(C_6H_{10}O_3P)].H_2O$ in which the two dimensional layers are connected to each other by weak van der waal interactions were studied. Few layer nanosheets of these materials were prepared by using a top-down approach. We have exfoliated these materials by simple and cost effective ultrasonication method to obtain the nanosheets. The nanosheets thus obtained were characterized with the help of atomic force microscopy. Nanosheets as thin as 3 nm were obtained. Variation in thickness and lateral dimension of the nanosheets with different duration of ultrasonication were investigated and was found that the thickness as well as lateral dimension of the nanosheets decreases with the increase in duration of ultrasonication. We have investigated the variation in magnetic properties of the nanosheets of $[(C_{10}H_{13}O_3P)Co(H_2O)]$ and $[(C_{10}H_{13}O_3P)Ni(H_2O)]$. Antiferromagnetic ordering which was present in the bulk phase disappears on exfoliation into few layers. Optical properties of $[Cu(C_8H_{10}O_3P)_2]_n$, $[Cu_6(H_2L)_3(H_2O)_{10}]_n.4H_2O$, $[Cu(C_6H_{10}O_3P)].H_2O$ and $[(C_{10}H_{13}O_3P)Cu(H_2O)]$ were also investigated. Charge transfer band in the photoluminescence spectra of these complexes show hypsochromic shift on exfoliation into nanosheets.

* *Paper based on this work has appeared in J. Solid State Chem. 2014* (http://dx.doi.org/10.1016/j.jssc.2014.02.020)

1.1 Introduction:

Hybrid inorganic-organic materials can be defined as compounds constituted by an infinite network of inorganic and organic moieties. The connectivity may be extended in one dimension to give one-dimensional (1 D) chains or in two or three dimensions to give two-dimensional (2 D) layers and three-dimensional (3 D) frameworks[1]. They can be broadly classified into two categories, *viz.* porous frameworks, often referred as metal-organic frameworks (MOFs), and dense frameworks. MOFs have attracted a great attention over the years owing to its catalytic, gas storage and separation properties[1-2] whereas dense frameworks which often incorporate metal-oxygen-metal (M-O-M) connectivity have gained interest because of their ability to exhibit cooperative behaviour, as in inorganic materials, to provide interesting properties like magnetic ordering and dielectric properties[3]. Majority of the research studies on hybrid materials are focussed on the investigations of single crystals and micron size polycrystalline materials. Of late various methods have been developed for the deposition of MOF thin films e.g. direct growth/deposition from solvothermal mother solutions, stepwise layer-by-layer growth onto a substrate, electrochemical deposition on metal substrates, gel-layer approaches and assembly of pre-formed nanocrystals[4]. Methods to fabricate MOF membranes have also been addressed recently[5]. However, most of these works are based on "bottom-up" approaches. "Top-down" approaches have already been very successfully employed to prepare graphene from graphite[6]. The successful isolation of graphene sheets along with the advancement in the field of scanning probe microscopies has triggered many research works devoted to isolation of 2D crystallites of inorganic materials like metal oxides, hydroxides and chalcogenides[7]. Recently there have been few reports on synthesis of nanosheets from layered MOFs as well. It has been shown that layered MOFs with weak interlayer interactions can be exfoliated into nanosheets by simple and cost-effective ultrasonication method[8].

1.2 Scope of Investigation:

Layered MOFs can be exfoliated into nanosheets by simple ultrasonication method. The properties of these nanosheets of MOFs have not been studied in detail yet.

We, therefore, have investigated the magnetic properties of nanosheets synthesized from bulk MOFs, which show magnetic ordering. Moreover, we have studied the effect on the absorption and photoluminescence properties which are introduced due to exfoliation of MOFs into few layer nanosheets.

1.3 Experimental Section:

1.3.1 Synthesis of MOFs:

The synthesis and characterization of bulk $[(C_{10}H_{13}O_3P)Co(H_2O)]$, $[(C_{10}H_{13}O_3P)Ni(H_2O)]$, $[(C_{10}H_{13}O_3P)Cu(H_2O)]$ $[Cu_6(H_2L)_3(H_2O)_{10}]_n.4H_2O$, $[Cu(C_8H_{10}O_3P)_2]_n$ and $[Cu(C_6H_{10}O_3P)].H_2O$ were carried out in collaboration with Prof. R. Murugavel, Department of Chemistry, Indian Institute of Technology, Mumbai. The synthesis procedure is listed, in brief, below:

a) $[(C_{10}H_{13}O_3P)Co(H_2O)]$ (1) :

0.249g (1mmol) of $Co(OCOCH_3)_2.H_2O$ was dissolved in 20mL methanol. The solution thus formed was added to a solution of mesityl-1-methylenephosphonic acid (0.214g, 1mmol) in methanol (10mL) with continuous stirring at room temperature. It immediately starts to precipitate to give blue color precipitate, which was then filtered and washed with water and methanol several times to remove any unreacted starting materials. It was then dried under vacuum to obtain pure crystals of $[(C_{10}H_{13}O_3P)Co(H_2O)]$.

b) $[Cu(C_8H_{10}O_3P)_2]_n$[9] (2):

Hexaaquocopper(II) perchlorate (0.372 g, 1.0 mmol) was added to a solution of N-benzoylphosphoradimic acid (H_2bpa) (0.201 g, 1.0 mmol) in methanol (30 mL) in one aliquot. The resulting solution was kept for stirring for 2 hr at room temperature after which it was filtered to remove precipitate that had formed. The clear blue solution was then kept at room temperature for crystallisation. Blue crystals of $[Cu(C_8H_{10}O_3P)_2]_n$ or $[Cu(Hbpa)_2]_n$ were obtained after 2 days.

c) $[Cu_6(H_2L)_3(H_2O)_{10}]_n.4H_2O$ (3):

0.130 g (0.32 mmol) of mesityl-1,3,5-tris(methylenephosphonic acid) or H_6L and 0.186 g (0.32 mmol) of hexaaquocopper(II) perchlorate were dissolved in 2 mL of deionized water with continuous stirring to give a light blue solution. The pH of this solution was adjusted to 4.0 by using 1M NaOH solution after which it was transferred to a Teflon-lined autoclave and heated in an oven kept at 110^oC for 3days. It was then cooled slowly to room temperature to obtain light green crystals which were collected. It was washed with cold methanol to remove any unreacted starting materials to obtain pure crystals of $[Cu_6(H_2L)_3(H_2O)_{10}]_n.4H_2O$.

d) $[(C_{10}H_{13}O_3P)Cu(H_2O)]$ (4):

0.199g (1mmol) of $Cu(OCOCH_3)_2.H_2O$ was dissolved in 20mL methanol. The solution thus formed was added to a solution of mesityl-1-methylenephosphonic acid (0.214g, 1mmol) in methanol (10mL) with continuous stirring at room temperature. It immediately starts to precipitate to give blue color precipitate, which was then filtered and washed with water and methanol several times to remove any unreacted starting materials. It was then dried under vacuum to obtain pure crystals of $[(C_{10}H_{13}O_3P)Cu(H_2O)]$.

e) $[(C_{10}H_{13}O_3P)Ni(H_2O)]$ (5):

0.248g (1mmol) of $Ni(OCOCH_3)_2.H_2O$ was dissolved in 20mL methanol. The solution thus formed was added to a solution of mesityl-1-methylenephosphonic acid (0.214g, 1mmol) in methanol (10mL) with continuous stirring at room temperature. It immediately starts to precipitate to give white color precipitate, which was then filtered and washed with water and methanol several times to remove any unreacted starting materials. It was then dried under vacuum to obtain pure crystals of $[(C_{10}H_{13}O_3P)Ni(H_2O)]$.

f) $[Cu(C_6H_{10}O_3P)].H_2O$ (6):

An aqueous solution of cyclohexyl phosphonic acid (0.164g, 1mmol) was added to a solution of $Cu(OCOCH_3)_2.H_2O$ (0.199g, 1mmol) in 10mL water with continuous stirring. The solution obtained was heated in a water bath for 1 h. The product obtained was filtered and washed several times with deionised water and then dried in a dessicator to get pure crystals of $[Cu(C_6H_{10}O_3P)].H_2O$.

1.3.2 Synthesis of nanosheets of bulk MOFs:

0.6 mg – 0.8 mg of compounds **1**, **2**, **3**, **4, 5** and **6** each were dispersed in 10 mL of ethanol. Each of them was sonicated in an ultrasonicator (Branson B3510E-MT, operating frequency – 40 kHz) for different durations (30 min, 1.5 hr, 3 hr) to obtain respective colloidal solutions.

1.3.3 Characterization:

The colloidal solutions obtained after sonication were characterized by Atomic Force Microscopy (AFM) in an Innova Atomic Force Microscope in the tapping mode. The solution was dispersed on a silicon substrate and the solvent was evaporated by keeping it overnight at room temperature. The UV-visible spectra of the bulk samples were recorded in Perkin Elmer lambda 700 in percentage reflectance mode whereas those of the colloidal solutions were recorded in Perkin Elmer lambda 650 in the absorbance mode. The photoluminescence spectra were recorded in Horiba Jobin Yvon – Fluorolog-3 spectrophotometer with Xe lamp as the source.

DC magnetization measurements were carried out in a Superconducting Quantum Interference Device that employs the technique of vibrating sample magnetometer (SQUID-VSM) (Magnetic Property Measurements System MPMS-3, Quantum Design, U.S.). Few milligram of bulk sample was packed in a piece of butter paper for the measurement. It was mounted and loaded in the sample chamber. After centring the sample within the detection coils, the measurement was started. The sample was first cooled to 2 K in the presence of an external magnetic field of strength 100 Oe. The

magnetization was then recorded with temperature up to 290 K. For the few layer nanosheets, the colloidal solution was drop-casted on a silicon substrate and the solvent was evaporated by keeping the sample under a lamp. The diamagnetic contribution from the butter paper and silicon substrate was subtracted accordingly to obtain the magnetization inherent of the samples.

1.4 Results and Discussion:

All the compounds have layered structure in which the 2 D sheets are linked together by weak van der Waal forces. This weak van der Waal interaction can be easily ruptured by applying some mechanical force. In our case, ultrasonication acts as the mechanical force.

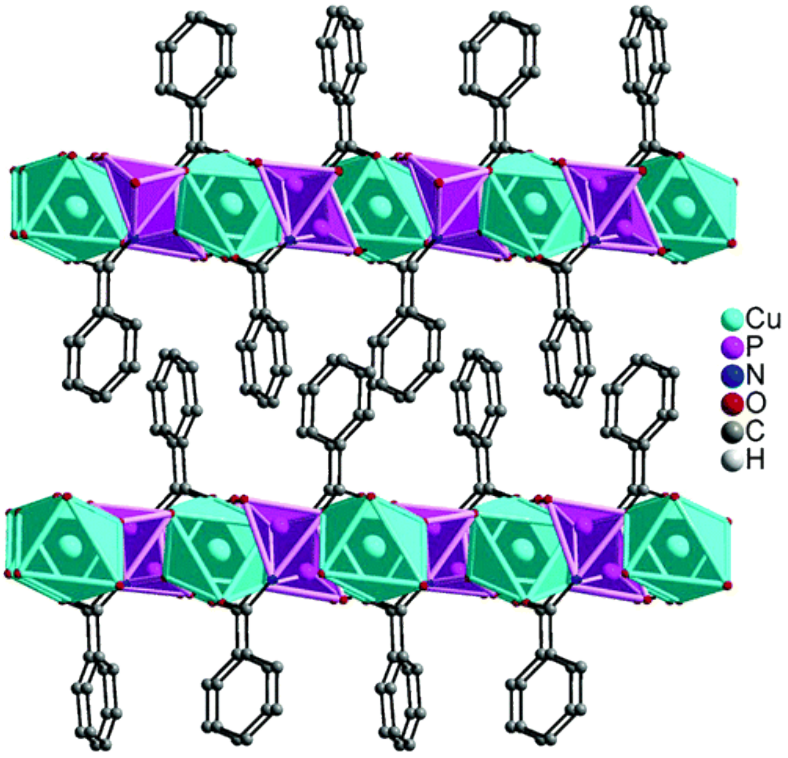

Fig 1.1 Layered structure of compound 3when viewed down the b axis (H atoms are omitted for clarity) Reprinted with permission from [9]. Copyright 2006 American Chemical Society

Figure 1.1 shows the layered structure of compound 2. The 2 D sheets of compound 2 are bound together by π-π interactions between the benzene rings of the adjacent layers.

1.4.1 Exfoliation into Nanosheets:

The colloidal suspensions of compounds 1, 2, 3, 4, 5 and 6 in ethanol, on shining a LASER beam, was found to scatter the incident light, thereby exhibiting tyndall effect. These colloidal suspensions were dispersed on a silicon substrate for imaging in Atomic Force Microscope (AFM).

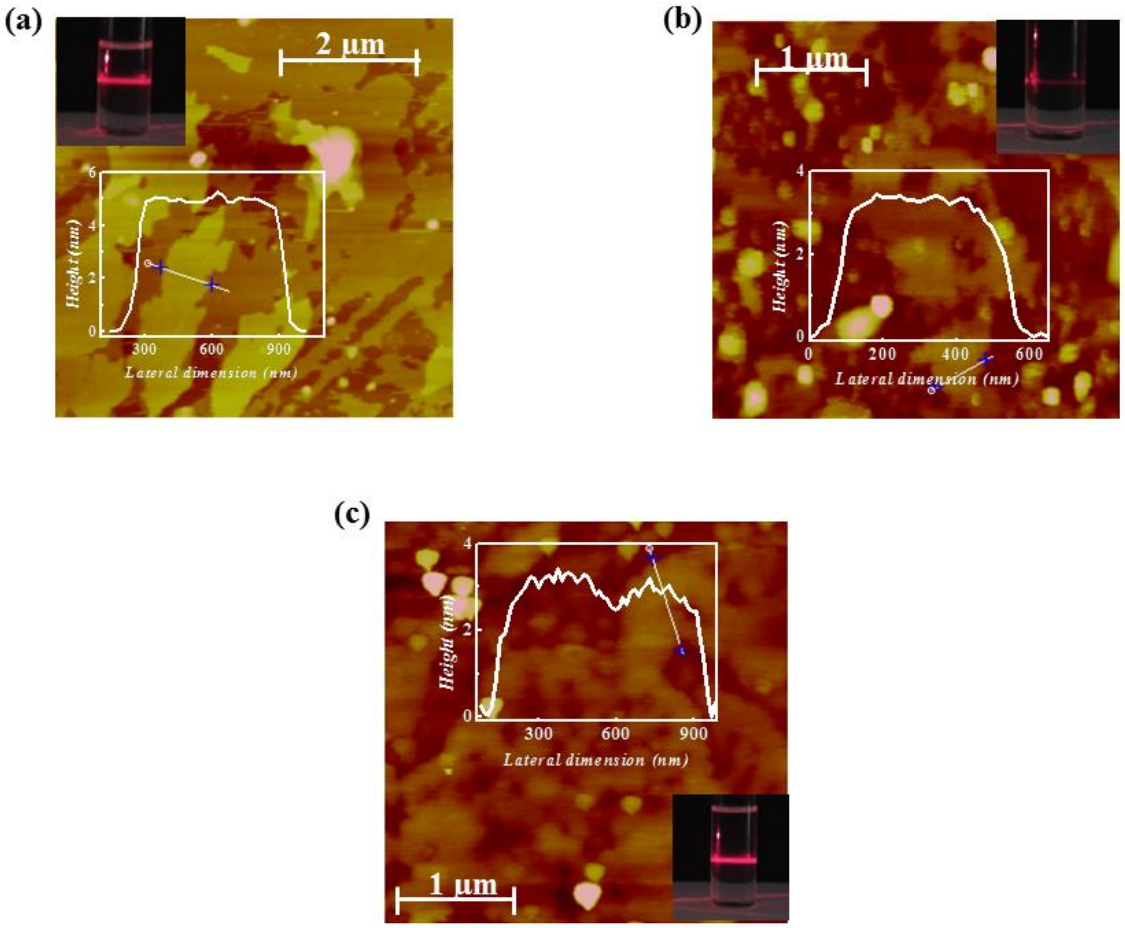

Figure 1.2 AFM images and tyndall cones of compound 1 after exfoliation (a) 30m (b) 1.5 hr (c) 3hr

From the AFM images of the nanosheets, shown in Figure 1.2, it can be said that the thickness of the nanosheets of compound 1, which were obtained after ultrasonication for 30 min, was around 5 nm which decreases to around 3 nm on increasing the duration of utrasonication to 1.5 hr to 3 hr. Moreover, on increasing the duration of ultrasonication, the lateral dimension of the nanosheets also decreases considerably. Similar observations

were found for the nanosheets obtained from the exfoliation of compound 2 and 3. Figure 1.3 shows the AFM images of the nanosheets of compound 2, 3, 4 and 5.

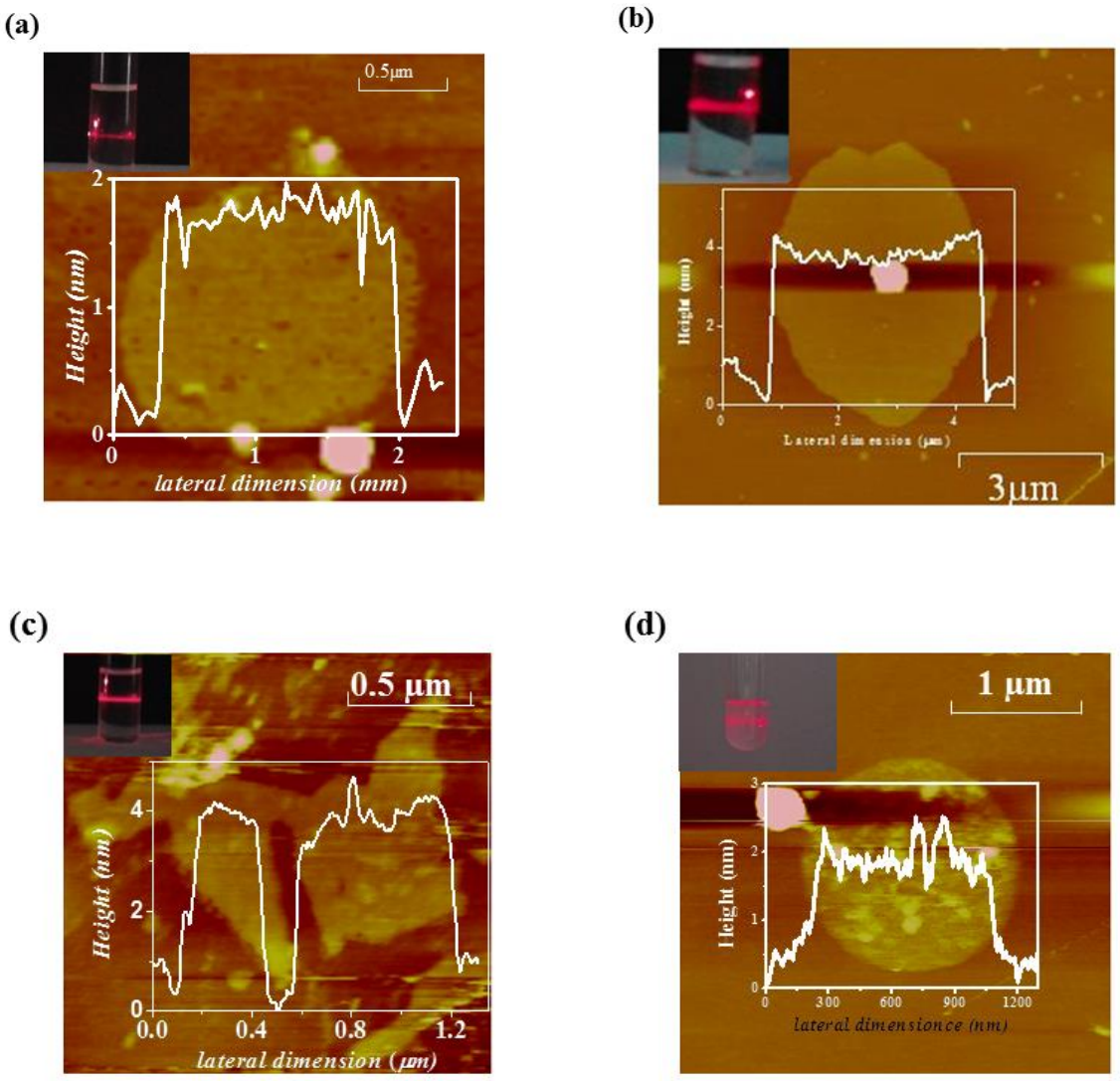

Figure 1.3 AFM images and tyndall cones of (a) compound 2 (b) compound 3 (c) compound 4 and (d) compound 5

1.4.2 Optical properties of $[Cu_6(H_2L)_3(H_2O)_{10}]_n.4H_2O$,$[Cu(C_8H_{10}O_3P)_2]_n$, $[Cu(C_{10}H_{13}O_3P)]_n$ and$[Cu(C_6H_{10}O_3P)]_n$:

The UV-visible absorption spectrum of $[Cu(C_8H_{10}O_3P)_2]_n$, denoted as compound **2**, shows mainly two bands (figure 1.4 (a)). The strong band that appears in the region 200 nm – 400 nm consists of mainly two bands, centred at 245 nm and 290 nm, merged together. The absorption peak at 245 nm can be attributed to intra-ligand charge transfer (ILCT) whereas the peak at 290 nm can be attributed to ligand to metal charge transfer (LMCT)[10]. The weak band observed in the region of 600 nm – 900 nm is due to d–d transition of Cu (II) ions. However, the colloidal solution obtained after exfoliation does not show the characteristic d–d peak (figure 1.4 (b)). It is probably due to the dilute nature of the solution[8c]. Moreover in the 200 nm – 400 nm region, only one peak appeared at 234 nm.

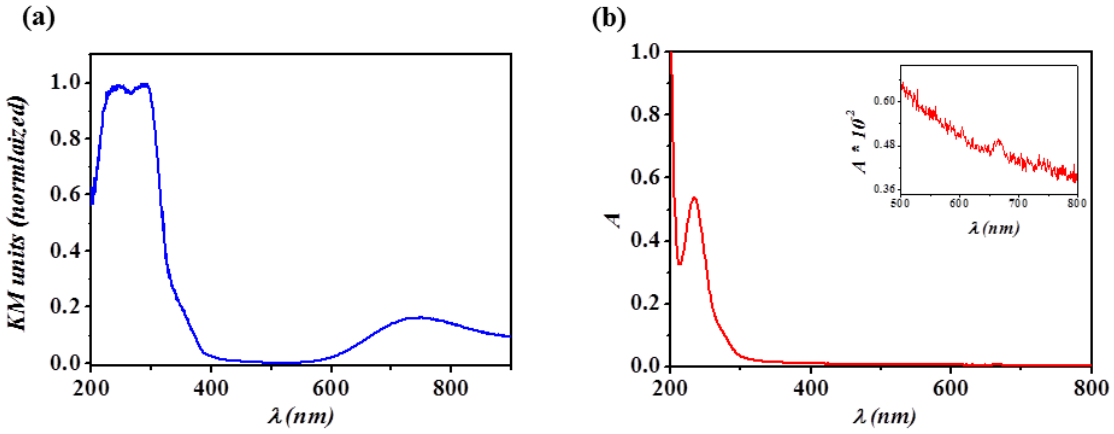

*Fig. 1.4 UV-visible spectra of (a) bulk compound **2** (b) nanosheets of compound **2***

The compound 2, on exciting at wavelength 250 nm, two emission bands were observed at 294 nm and 398 nm (figure 1.5). The emission spectrum of few layers of compound **2** shows a hypsochromic shift of the emission band at 398 nm to 347 nm as shown in figure 1.5. This hypsochromic shift may be attributed to the reduction in the strength of π-π interaction between the layers after being exfoliated into few layer nanosheets.

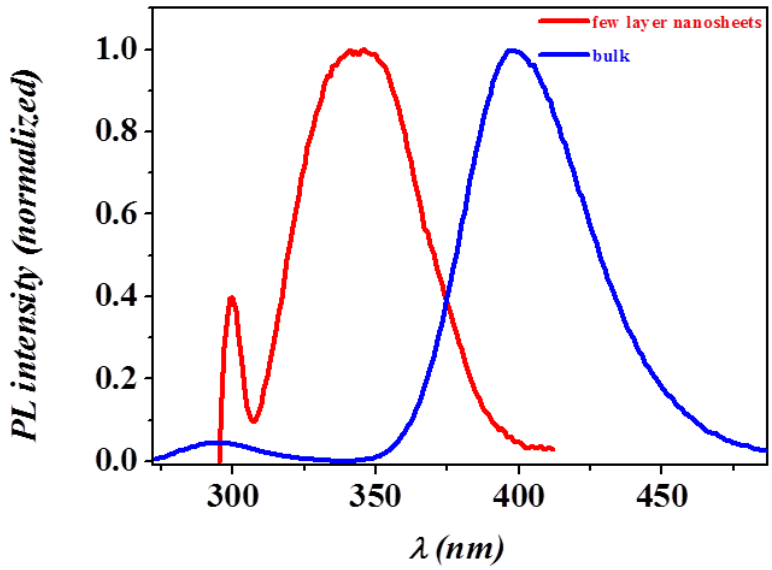

*Fig. 1.5 Photoluminescence spectra of bulk and few layer nanosheets of compound **2***

$[Cu_6(H_2L)_3(H_2O)_{10}]_n.4H_2O$, denoted as compound **3,** also shows two broad absorption bands in the UV-visible spectra as shown in figure 1.6(a). Similar to compound **2**, the absorption band in the region 200nm – 500 nm may be attributed to ILCT and LMCT whereas the band in the region 500 nm – 900 nm is due to Cu (II) ion d–d transition. This d–d transition absorption band was not observed in the UV-visible spectrum of the colloidal solution of compound **3** for the similar reason cited above. From figure 1.6(b), it can be said that light scattering contribute strongly to the observed behaviour of the colloidal solution.

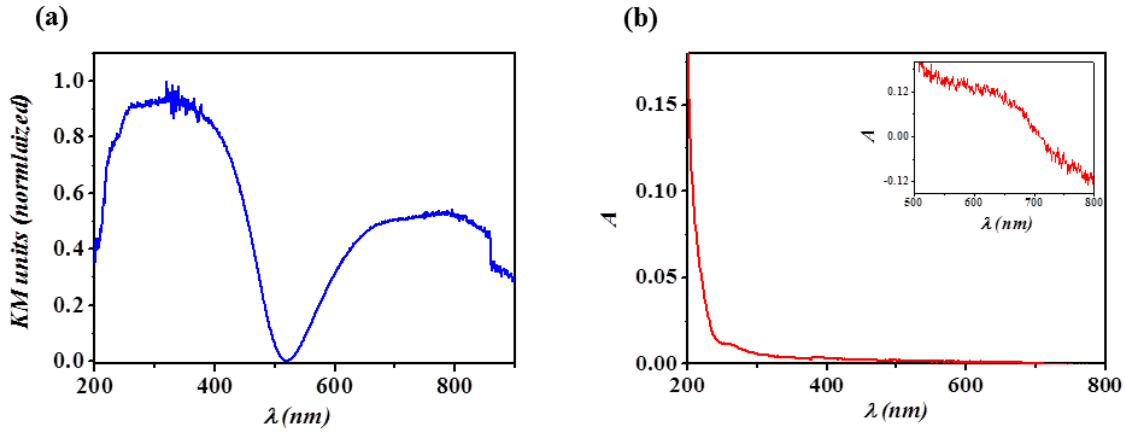

*Fig. 1.6 UV-visible spectra of (a) bulk compound **3** (b) nanosheets of compound **3***

Similar to compound **2**, compound **3** was also excited at 250 nm. The emission spectrum shows two emission bands at 294 nm and 398 nm. The emission band at 398 nm undergoes hypsochromic shift to 346 nm on exfoliating into few layer nanosheets (figure 1.7).

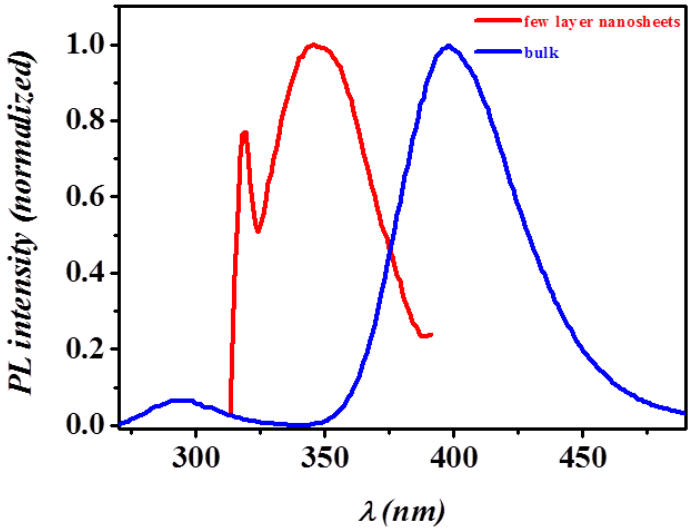

*Fig. 1.7 Photoluminescence spectra of bulk and few layer nanosheets of compound **3***

$[(C_{10}H_{13}O_3P)Cu(H_2O)]_n$, denoted as compound 4, like compound 2 and 3 shows two broad absorption bands in the region 200 nm – 500 nm that corresponds to ILCT and LMCT and 500 nm – 900 nm (figure 1.8(a)) that corresponds to d-d transition of Cu (II) ions. The d-d transition band of Cu (II) ions is very weak in the UV-visible absorption spectra of the colloidal solution of compound 4 (figure 1.8(b)).

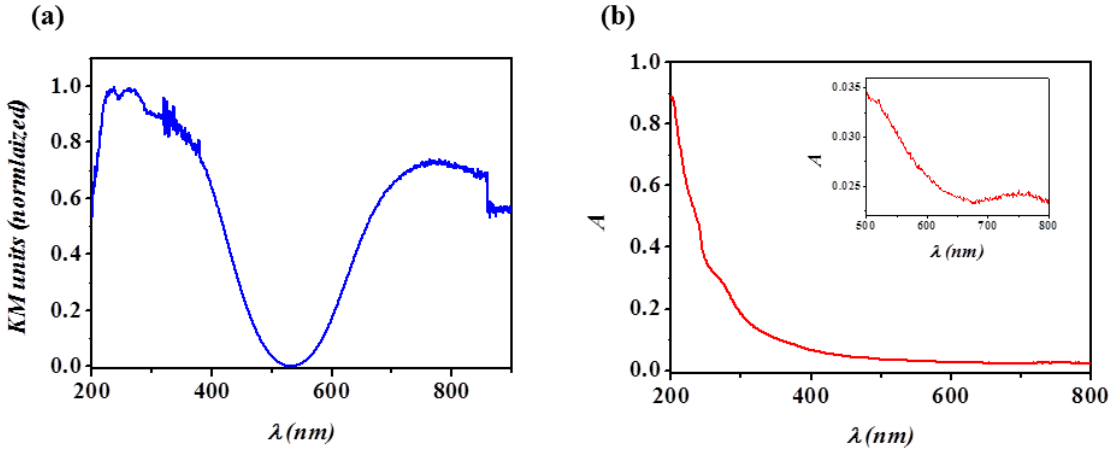

*Fig. 1.8 UV-visible spectra of (a) bulk compound **4** (b) nanosheets of compound **4***

The UV-visible absorption spectra of $[Cu(C_6H_{10}O_3P)].H_2O$, denoted as compound 5, shows two peaks centred at 248 nm and 795 nm (figure 1.9(a)). The peak at 248 nm corresponds to intra-ligand charge transfer (ILCT) and the peak at 795 nm is due to characteristic d-d transition of Cu (II) ions. On exfoliating into nanosheets, it was observed that the d-d absorption peak has significantly reduced similar to the other Cu-complexes studied.

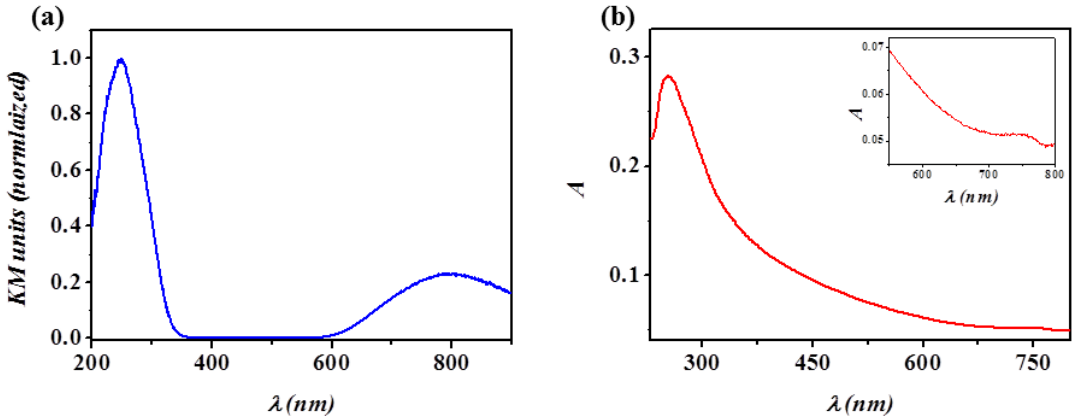

*Fig. 1.9 UV-visible spectra of (a) bulk compound **5** (b) nanosheets of compound **5***

1.4.2 Magnetic properties of $[(C_{10}H_{13}O_3P)Co(H_2O)]$ (ψ_1) and $[(C_{10}H_{13}O_3P)Ni(H_2O)]$ (ψ_2):

The DC magnetization of $[(C_{10}H_{13}O_3P)Co(H_2O)]$, denoted as compound $\boldsymbol{\psi_1}$, was measured under field-cooled (FC) conditions in the presence of a magnetic field of strength 100 Oe. Figure 1.10(a) shows the variation of molar magnetic susceptibility χ_M with temperature T. It is clear that compound $\boldsymbol{\psi_1}$ undergoes antiferromagnetic ordering below the Néel temperature T_N = 9. 5 K. The Curie-Weiss constant θ_{CW} was found to be -14.48 K. The effective paramagnetic moment per Co atom was obtained as 4.07μ_B.

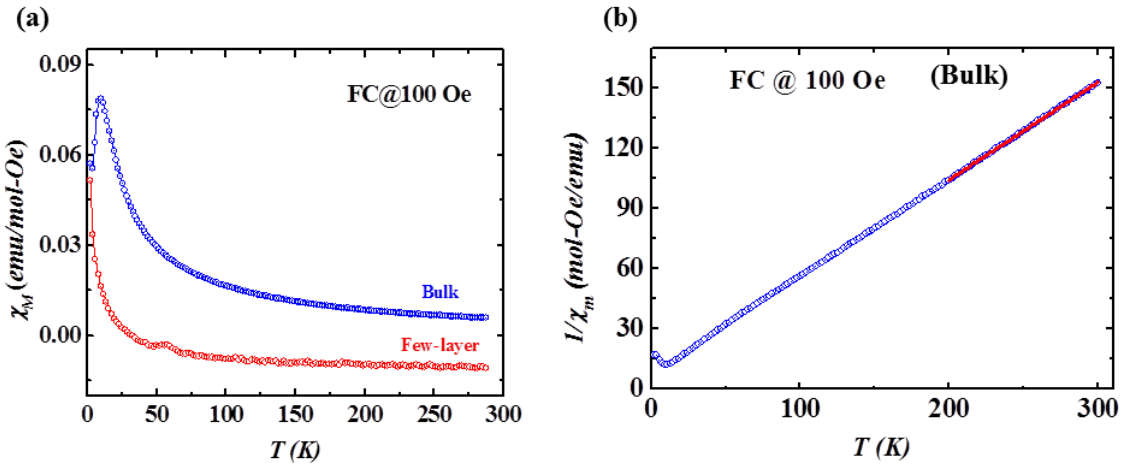

Fig. 1.10 (a) Variation of molar magnetic susceptibility with temperature for bulk and few layer nanosheets of compound $\boldsymbol{\psi_1}$ *(b) Variation of inverse molar susceptibilty with tempertaure for bulk compound* $\boldsymbol{\psi_1}$

On measuring the magnetization of compound $\boldsymbol{\psi_1}$ after exfoliation into nanosheets, no antiferromagnetic transition peak was observed. It rather shows a paramagnetic behaviour (figure 1.10(a)). This is as expected as long range ordering cannot occur in the few-layer sample.

DC magnetization of $[(C_{10}H_{13}O_3P)Ni(H_2O)]$, denoted as compound $\boldsymbol{\psi_2}$, under FC conditions in the presence of an applied field of 100 Oe, shows that it undergoes antiferromagnetic ordering below T_N = 6 K (figure 1.11(a)). The Curie-Weiss constant θ_{CW} was found to be -225 K. The spin-only paramagnetic moment per formula unit was obtained as $5.03\mu_B$. On exfoliating into nanosheets, the antiferromagnetic transition peak is less pronounced as long range ordering is less likely in few layer nanosheets (figure 1.11(a)).

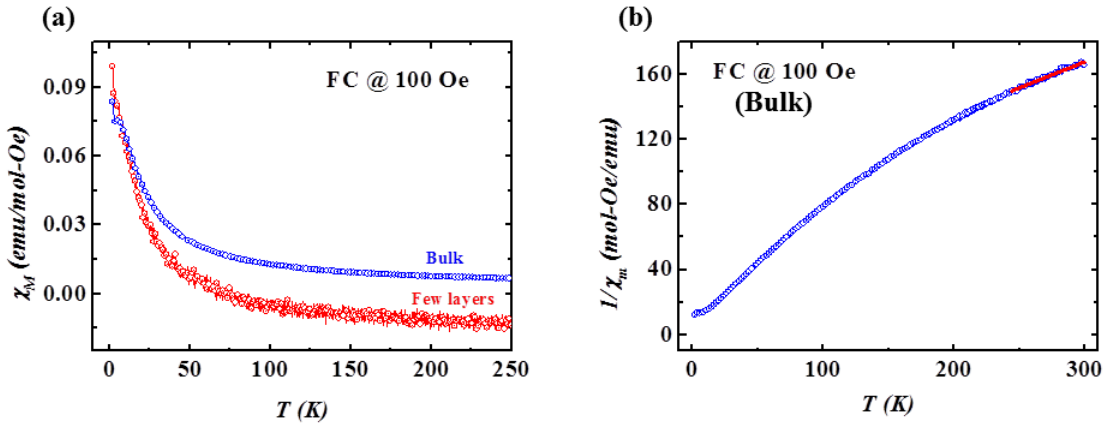

Fig. 1.11 (a) Variation of molar magnetic susceptibility with temperature for bulk and few layer nanosheets of compound ψ_2 *(b) Variation of inverse molar susceptibilty with tempertaure for bulk compound* ψ_2

1.5 Conclusion:

We have prepared few layer nanosheets by simple exfoliation using ultrasonication method. The thickness and lateral dimension of the nanosheets can be tuned by changing the duration of ultrasonication. With the increase in duration, the thickness as well as the lateral dimension decreases. We were able to obtain nanosheets as thin as 3 nm. We have observed a marked difference in the optical properties as well as the magnetic properties of the nanosheets from the bulk compound. $[(C_{10}H_{13}O_3P)Co(H_2O)]$, which is an antiferromagnet, becomes paramagnet on exfoliation into nanosheets. Antiferromagnetic ordering temperature of $[(C_{10}H_{13}O_3P)Ni(H_2O)]$ was found to be less pronounced on exfoliation. Nanosheets of $[Cu(C_8H_{10}O_3P)_2]_n$ and $[Cu_6(H_2L)_3(H_2O)_{10}]_n.4H_2O$ were found to exhibit hypsochromic shift of the charge transfer band.

1.6 References:

[1] A. K. Cheetham, C. N. R. Rao, R. K. Feller, *Chem. Comm.* **2006**, 4780-4795.

[2] J. Lee, O. K. Farha, J. Roberts, K. A. Scheidt, S. T. Nguyen, J. T. Hupp, *Chem. Soc. Rev.* **2009**, *38*, 1450-1459.

[3] C. N. R. Rao, A. K. Cheetham, A. Thirumurugan, *J. Phys.: Condens. Mat.* **2008**, *20*, 083202.

[4] O. Shekhah, J. Liu, R. A. Fischer, C. Woll, *Chem. Soc. Rev.* **2011**, *40*, 1081-1106.

[5] J. Gascon, F. Kapteijn, *Angew. Chem. Int. Edit.* **2010**, *49*, 1530-1532.

[6] (a) M. J. Allen, V. C. Tung, R. B. Kaner, *Chem. Rev.* **2009**, *110*, 132-145; (b) S. Stankovich, D. A. Dikin, R. D. Piner, K. A. Kohlhaas, A. Kleinhammes, Y. Jia, Y. Wu, S. T. Nguyen, R. S. Ruoff, *Carbon* **2007**, *45*, 1558-1565.

[7] R. Mas-Balleste, C. Gomez-Navarro, J. Gomez-Herrero, F. Zamora, *Nanoscale* **2011**, *3*, 20-30.

[8] (a) J.-C. Tan, P. J. Saines, E. G. Bithell, A. K. Cheetham, *ACS Nano* **2011**, *6*, 615-621; (b) P.-Z. Li, Y. Maeda, Q. Xu, *Chem. Comm.* **2011**, *47*, 8436-8438; (c) P. J. Saines, M. Steinmann, J.-C. Tan, H. H. M. Yeung, W. Li, P. T. Barton, A. K. Cheetham, *Inorg. Chem.* **2012**, *51*, 11198-11209; (d) P. J. Saines, J.-C. Tan, H. H. M. Yeung, P. T. Barton, A. K. Cheetham, *Dalton Trans.* **2012**, *41*, 8585-8593.

[9] R. Murugavel, M. P. Singh, *Inorg. Chem.* **2006**, *45*, 9154-9156.

[10] M. Shukla, N. Srivastava, S. Saha, T. R. Rao, S. Sunkari, *Polyhedron* **2011**, *30*, 754-763.

CHAPTER 2

Introduction to Magnetic Materials

The discovery of magnetite (Fe_3O_4), the first magnetic material known to man, marked the birth of magnetism. It was known to mankind more than 2500 years ago that this mineral has the power to attract pieces of iron. The word “magnet” comes from a Greek word similar to Magnesia, the district where huge deposits of the mineral was found.

The first truly scientific study of magnetism was carried out by William Gilbert in the sixteenth century. But it was in the late nineteenth and early twentieth century that the field of magnetism began to flourish with some really great contributions from Curie, Langevin and Weiss. Since then many new materials with interesting magnetic properties have been developed. These magnetic materials find wide applications in the field of data storage and spintronic devices.

Magnetic materials can be broadly classified into 5 types on the basis of the ordering of magnetic moments, *viz.*:

1. Diamagnetic
2. Paramagnetic
3. Ferromagnetic
4. Antiferromagnetic
5. Ferrimagnetic

Before understanding these different types of materials, it is necessary to know the origin of magnetic moments.

2.1 Origin of Magnetism:

The magnetic moment of an atom is due to:

1. electrons circulating within the orbital giving rise to orbital angular momenta
2. spinning of electron about its own axis giving rise to spin angular momenta

The magnitude of the orbital contribution to the magnetic moment is given by:

$m = \mu_B\sqrt{l(l+1)}$, where l = angular momentum quantum number

μ_B = Bohr magneto

$= \frac{e\hbar}{2m_e}$

$= 9.274 \times 10^{-24}\ J/T$

The magnitude of the spin contribution to magnetic moment is given by:

$m = g_e\mu_B\sqrt{s(s+1)}$, where s = spin quantum number

g_e = g-factor of electron

$= 2.002319 \approx 2$

The magnetic moment due to spin of electrons interacts with the magnetic field generated by the orbital motion. This interaction is known as spin-orbit coupling. In light atoms spin-orbit coupling is very weak and therefore, it is the spin-spin coupling and orbit-orbit coupling that contributes to the total angular momentum of an atom, whereas in the case of heavy atoms like lanthanides and actinides, spin-orbit coupling is very strong. The total magnetic moment, thus, is given by:

$m = g\mu_B\sqrt{J(J+1)}$, where J = total angular momentum quantum number

g = Landé g-factor

The spin-only magnetic moment of an atom i.e. the effective magnetic moment μ_{eff} (neglecting the orbital moment contribution) is given by:

$$\mu_{eff} = 2\sqrt{S(S+1)}\mu_B \,, \quad \text{where } S = \text{total spin quantum number}$$

2.2 Types of Magnetic Materials:

2.2.1 Diamagnetic materials:

Change in orbital motion of electrons due to an applied magnetic field is known as diamagnetic effect. It occurs in all atoms but diamagnetism is a very weak phenomenon that only those atoms with filled shells and therefore which have no net magnetic moments are classified as diamagnetic materials. All of the noble gases are diamagnetic.

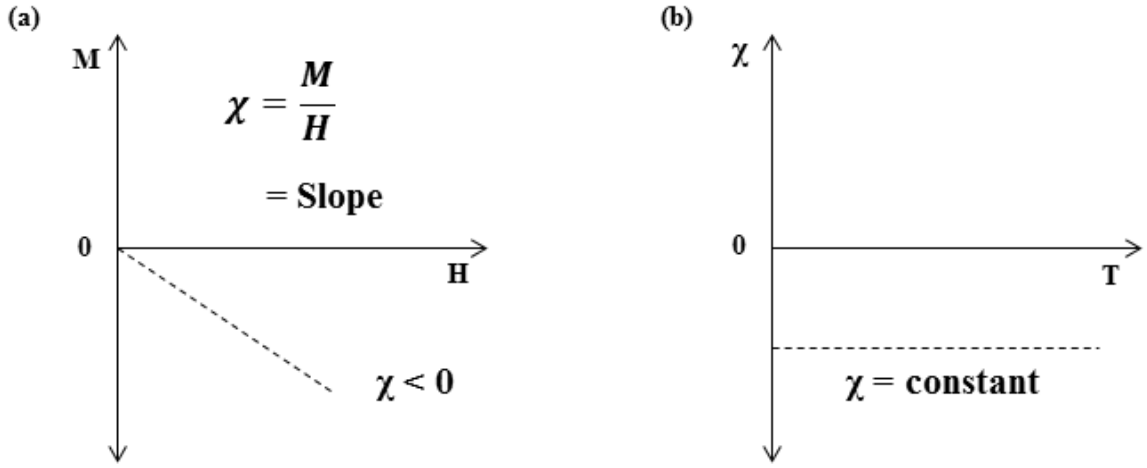

Fig 2.1 (a) Variation of magnetization with an applied magnetic field (b) variation of magnetic susceptibility with temperature for diamagnetic materials

In diamagnetic materials, the magnetic flux density Φ is less inside the material. The slope of magnetization *M vs. H* (magnetic field) curve i.e. magnetic susceptibility χ is negative and also independent of temperature.

2.2.2 Paramagnetic Materials:

For a material to show paramagnetism, it is necessary to have one or more unpaired electrons. The magnetic dipoles are only weakly coupled and hence are

randomly oriented. Therefore the net magnetization is zero in the absence of an applied magnetic field. But when a magnetic field is applied, a small fraction of the moments are deflected into the field direction.

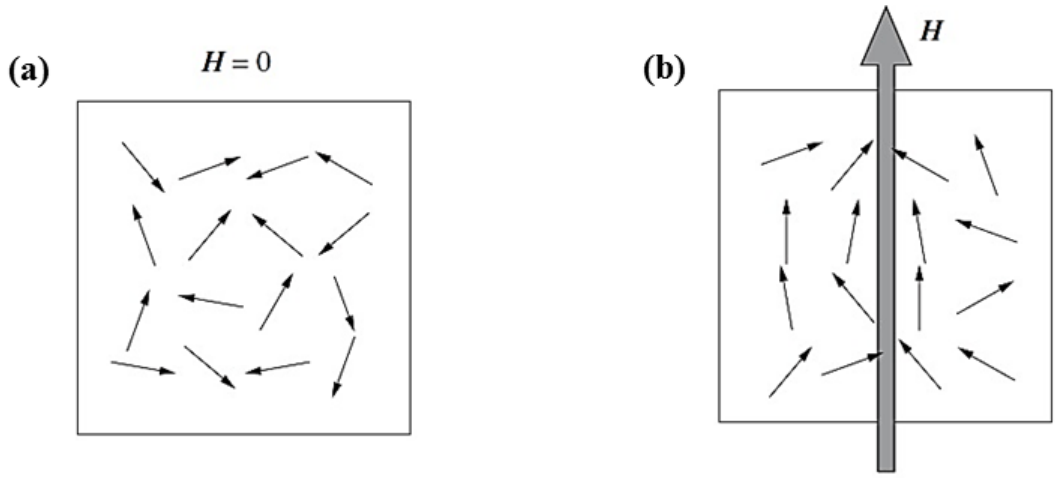

Fig 2.2 Schematic showing the alignment of magnetic moments (a) in the absence of an applied field (b) in the presence of an applied field

In 1895, French physicist Pierre Curie showed that for paramagnetic materials susceptibility is inversely proportional to absolute temperature.

$$\text{i.e} \quad \chi = \frac{C}{T} \quad , \qquad \text{where } C = \text{Curie Constant}$$

This is known as Curie's law. The temperature dependence of susceptibility can be explained by Langevin theory that assumes that magnetic moments on atomic sites are non-interacting and are randomly oriented due to their thermal energy. According to this theory, the orientation of localized atomic magnetic moments, on applying an external magnetic field, shifts along the direction of the field. But it was found that many paramagnetic materials do not obey this Curie's law. Weiss later postulated the existence of an internal interaction between the localized magnetic moments and he called this as "molecular field". Assuming molecular field H_w to be directly proportional to the magnetisation, he modified the Curie's law to give a more general equation known as Curie-Weiss law:

$$\chi = \frac{C}{T-\theta} \quad , \qquad \text{where } \theta = \text{Weiss Constant}$$

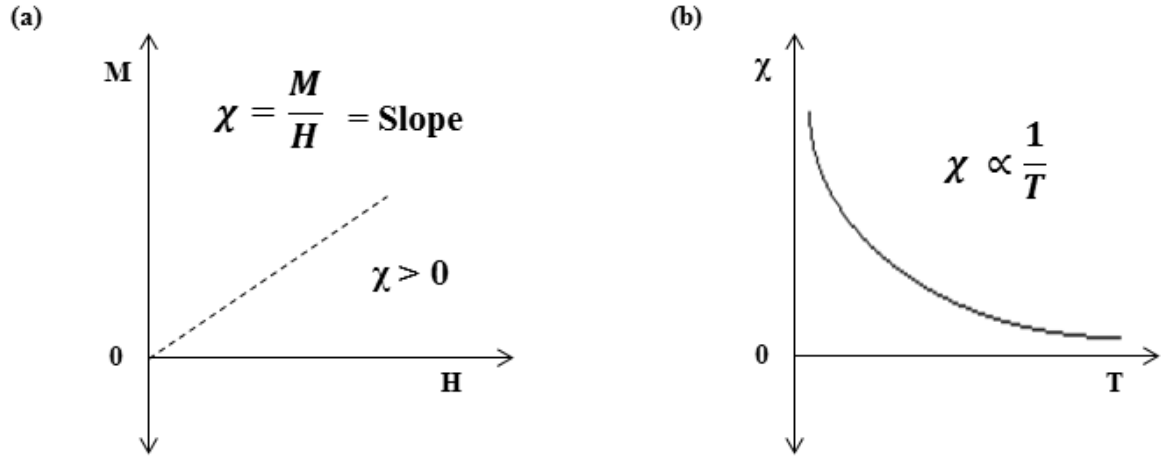

Fig 2.3 (a) Variation of magnetization with an applied magnetic field (b) variation of magnetic susceptibility with temperature for diamagnetic materials

Though Langevin theory explains the temperature dependence of susceptibility for most paramagnetic materials, it fails to explain the behavior of paramagnetic metals in which susceptibility is more or less independent of temperature –phenomenon known as *Pauli paramagnetism*. This phenomenon can be explained by band theory.

In paramagnetic metals, the energy states for up-spin and down-spin electrons are same and therefore, the energy levels at the Fermi energy E_F are identical for both the states. However, on applying magnetic field, the band containing the electrons with magnetic moments aligned parallel to the field has a lower energy by an amount $\mu_B H$ and the band containing electrons with moments aligned antiparallel to field has higher energy by the same amount. As a result, antiparallel magnetic moments try to reorient themselves parallel to the field. It is possible only by moving into the vacant parallel-moment states. For low-lying electrons, the energy gained by realignment would be outweighed by the energy required to promote these electrons to the vacant state. Therefore, only those electrons whose energy is close to E_F have sufficient energy for the realignment.

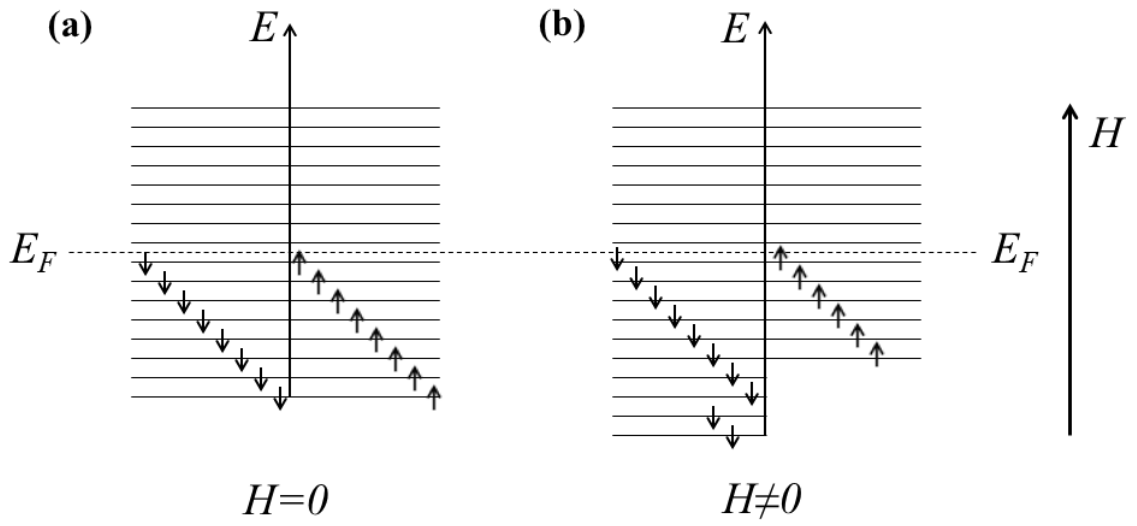

Fig. 2.4 Schematic of electronic states in a free-electron gas when (a) no external magnetic is applied (b) field is applied

Total susceptibility of Pauli paramagnetic materials is given by:

$$\chi = \frac{\mu_o \mu_B^2 (N/V)}{E_F}$$

2.2.3 Ferromagnetic materials:

In ferromagnetic materials, the magnetic moments interact very strongly *via* exchange interaction forcing them to align parallel to each other.

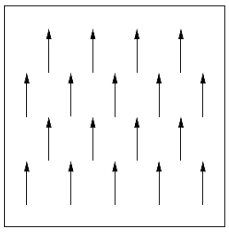

Fig 2.5 Schematic of magnetic moments ordering in ferromagnetic materials

It should be noted that the net magnetization is zero in the absence of an applied magnetic field. This is due to the formation of magnetic domains to minimize the magnetic energy of the system. In each domain all the spins are aligned parallel but different domains have different spin orientations.

When magnetic field is applied, the domain whose magnetization is closest to the field direction starts to grow at the expense of other domains. Eventually the applied field is sufficient to eliminate all the domain walls and a single domain is formed (figure 2.6(a)). Further increase in magnetization occurs by rotating the magnetic dipoles from the easy axis into the direction of the applied field. Large field is required to reach saturation magnetization in case of systems having large magnetocrystalline anisotropy.

When the magnetic field is removed, the dipoles rotate back to its easy axis of magnetization thereby decreasing the net magnetic moment along the field direction. The demagnetizing field then initiates growth of reverse domains to demagnetize the sample. But the demagnetizing field is not strong enough to overcome the energy barriers encountered when the domain walls intersect crystal imperfections. As a result, domain walls are not able to fully reverse its motion and hence, the magnetization curve shows hysteresis and some magnetization remains in the sample. This is known as remanence or remanent magnetization (M_r). An additional field has to be applied in reverse direction to reduce the magnetization to zero. This field is known as coercive field (H_c).

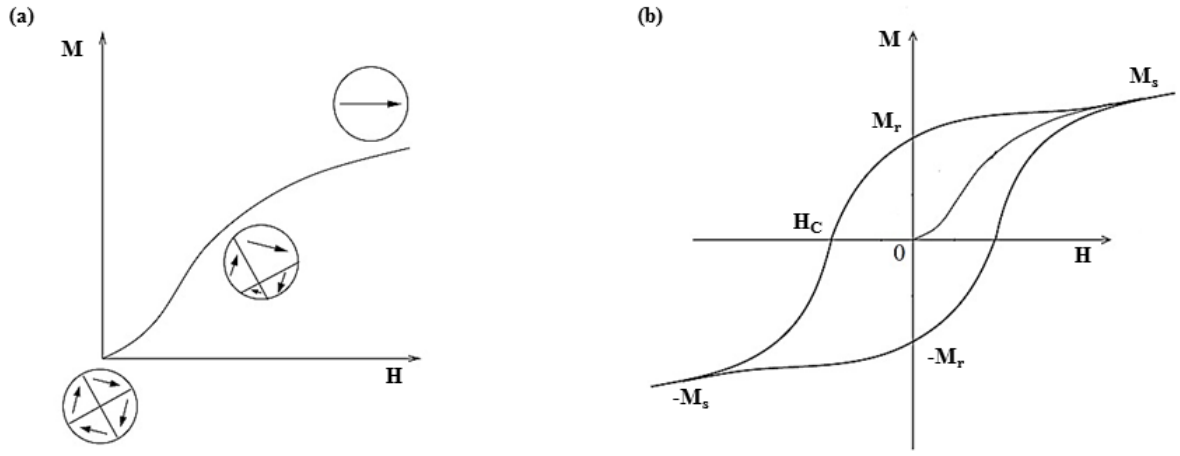

Fig 2.6 (a) Change in domain structure during magnetization and (b) hysteresis loop for a ferromagnetic material (adapted from [2])

Materials with high remanence and large coercive field are known as hard magnetic materials and are used as permanent magnets whereas materials with small remanence and small coercive fields are known as soft magnetic materials and are used in electromagnets and transformer cores.

Ferromagnetic materials become paramagnetic above a critical temperature known as Curie temperature (T_c). Above this temperature the thermal energy outweighs the exchange interaction causing randomization of the spins. The susceptibility follows the Curie-Weiss law with positive value of θ.

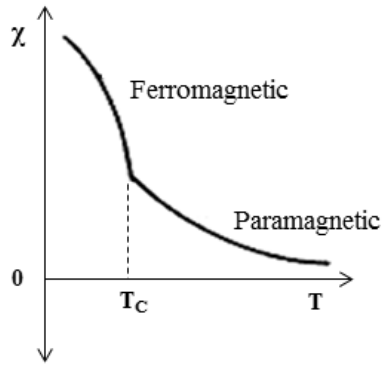

Fig 2.7 Variation of magnetic susceptibility with temperature for a ferromagnetic material

Weiss molecular field theory combined with Langevin theory of localized moments can explain many properties of ferromagnetic materials. However, it fails to account for the observed magnetic moment per atom in ferromagnetic materials, ferromagnetic metals in particular. To explain this behaviour, Stoner[1] proposed a model based on band theory known as "*collective-electron theory*". This concept was earlier discussed to explain Pauli paramagnetism.

In transition elements, when N atoms are brought together to an equilibrium interatomic distance do to form a solid, the outermost 3d and 4s electron clouds overlap and the corresponding levels undergoes splitting and form 3d and 4s bands respectively. The inner core electrons remain unaffected. 4s electrons being farther from the nucleus, form a broad band with low density of states whereas 3d band is narrow and has high density of states. It is assumed that the shape of these bands does not change markedly across the first transition series. This is known as *rigid band model*. In ferromagnetic transition metals like Fe, Co and Ni, E_F lies in the region of overlapping 3d and 4s bands. The 3d band being narrow has a much higher density of states at the Fermi level. As a result, the minimization in the exchange energy of electrons outweighs the amount of energy which is required to promote a 3d electron into a vacant state and reverse its spin.

This leads to spin unbalance in the 3d band. The resulting band structure is similar to that of Pauli paramagnetism with the only difference being the exchange interaction and not an external field that brings about the change in the band energy.

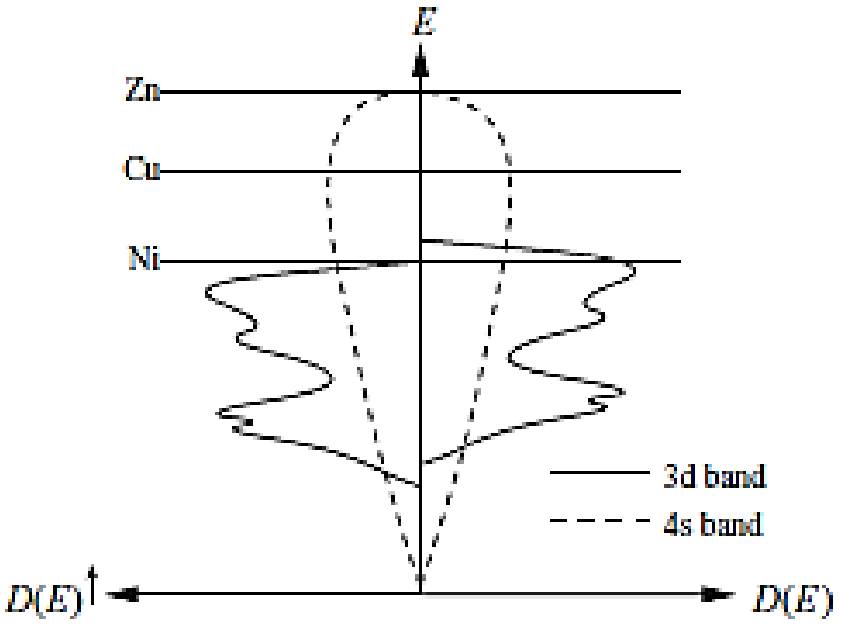

Fig 2.8 Schematic of 3d and 4s up-spins and down-spins density of states in transition metal (considering exchange interaction) (taken from[2])

2.2.4 Antiferromagnetic materials:

In antiferromagnetic materials, the interaction between the magnetic moments tends to align the adjacent moments anti-parallel to each other.

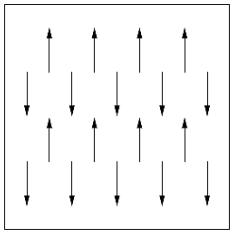

Fig 2.9 Schematic of magnetic moments ordering in antiferromagnetic materials

Antiferromagnets become paramagnet above a critical temperature known as Néel temperature (T_N). Above this temperature, they follow Curie-Weiss law with negative value of θ.

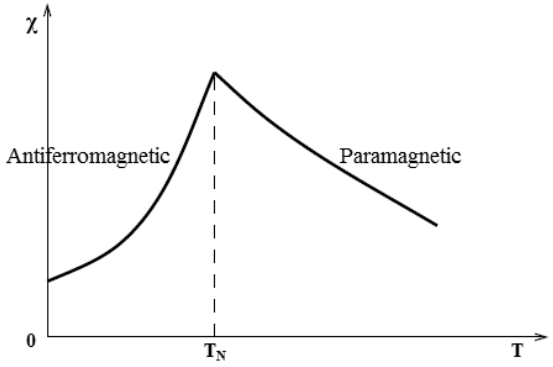

Fig 2.10 Variation of magnetic susceptibility with temperature for an antiferromagnetic material

Néel developed the theory of antiferromagnetism in 1948[3]. According to his theory, a lattice can be divided into two identical sublattices containing atoms A and B respectively. Assuming the most important interactions are the nearest neighbour interactions A-B, there exist two Weiss molecular fields.

The Weiss field H_W^A acting on sublattice A is proportional, but in the opposite direction, to the magnetization of sublattice B (M_B) and is given by:

$$H_W^A = -\gamma M_B \tag{1.1}$$

Similarly,

$$H_W^B = -\gamma M_A \tag{1.2}$$

For paramagnetic materials, Curie law gives $\chi = \frac{M}{H} = \frac{C}{T}$

$$\Rightarrow M = \frac{HC}{T}$$

Therefore,

(a) At $\boldsymbol{T > T_N}$ (paramagnetic region),

$$M_A = \frac{(H+H_W^A)C'}{T}$$ (H = applied magnetic field)

$$\Rightarrow M_A = \frac{(H-\gamma M_B)C'}{T} \tag{1.3}$$

Similarly, $$M_B = \frac{(H-\gamma M_A)C'}{T} \tag{1.4}$$

Solving eqns. (1.3) and (1.4), simultaneously to obtain M_A and M_B values, total magnetization M is thus obtained as:

$$M = \frac{2C'H}{T+C'\gamma}$$

which on rearranging gives $\frac{M}{H} = \frac{2C'}{T+C'\gamma} \Rightarrow \chi = \frac{C}{T+\theta}$, where $C = 2C'$ and $\theta = C'\gamma$

$$\Rightarrow \chi = \frac{C}{T-(-\theta)}$$

which is the Curie-Weiss law with negative value of θ.

(b) At $\boldsymbol{T < T_N}$:

The susceptibility of antiferromagnetic materials depends on the direction of the applied magnetic field. Considering the two limiting cases:

i. When H is parallel to M_A or M_B:

If H is applied parallel to the direction of M_A, then M_A will increase by a small amount δM_A whereas M_B will decrease by an amount δM_B. This will lead to a net magnetization and susceptibility is given by:

$$\chi_{\parallel} = \frac{2Nm^2B'(J,\alpha)}{2k_BT + Nm^2\gamma B'(J,\alpha)}$$

Where N = number of atoms per unit volume

m = magnetic moment of an atom

$B'(J,\alpha)$= derivative of Brillouin function w.r.t. α

ii. When H is perpendicular to M_A and M_B:

In this case, the applied magnetic field forces the magnetic moments to rotate such that a net magnetization is observed along the field direction. The susceptibility is given by:

$$\chi_{\perp} = \frac{1}{\gamma}$$

For a polycrystalline sample which has no preferred orientation, susceptibility is given by:

$$\chi_p = \frac{1}{3}\chi_{\parallel} + \frac{2}{3}\chi_{\perp}$$

(c) At $\boldsymbol{T = T_N}$:

$$\chi_{\parallel} = \chi_{\perp}$$

$$\therefore\ \chi_p = \chi_{\perp}$$

(d) At **T = 0K**:

$$\chi_{\parallel} = 0$$

$$\therefore\ \chi_p = \frac{2}{3}\chi_{\perp}$$

2.2.5 Ferrimagnetic materials:

In ferrimagnetic materials, similar to antiferromagnets, the adjacent magnetic moments are aligned antiparallel to each other but the magnetization of one sublattice of magnetic ions is greater than that of the oppositely oriented sublattice. Therefore, they possess a net spontaneous magnetization value.

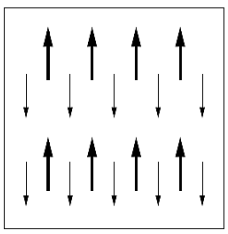

Fig 2.11 Schematic of magnetic moments ordering in ferrimagnetic materials

The magnetization curve of ferrimagnetic materials shows hysteresis, like ferromagnets, in the presence of a magnetic field.

Néel developed the theory of ferrimagnetism along with the theory of antiferromagnetism[3]. In ferrimagnets, A and B sublattices are not structurally identical and besides the nearest neighbour A-B interactions which tend to align the moments in the two sublattices antiparallel, A-A and B-B ferromagnetic interactions need to be taken into account to explain the behaviour of ferrimagnets.

2.3 Magnetic Anisotropy:

2.3.1 Magnetocrystalline Anisotropy:

Magnetocrystalline anisotropy is an intrinsic property of a material. It can be defined as the tendency of magnetization to align itself along a preferred crystallographic axis known as easy axis. This phenomenon is observed mainly due to spin-orbit coupling. The spin magnetic moment couples with the orbital motion which is, in turn, coupled very strongly to the lattice. So when a magnetic field tries to orient the magnetization along the field direction, the orbital also needs to be reoriented along with the spin. As a result, the magnetization resists such a reorientation and a large magnetic field needs to be applied to align the magnetization along the field direction. Magnetocrystalline anisotropy is very strong in rare earth materials.

The difference in energy per unit volume of a sample magnetized along the easy axis and hard axis is known as magnetocrystalline anisotropy energy.

2.3.2 Shape Anisotropy:

It is the phenomenon in which the magnetization prefers to align along the longer axis of a non-spherical particle. It can be explained from the concept of demagnetizing field H_d which acts in the direction opposite to the applied field.

$$H_d = N_d M, \qquad \text{where } N_d = \text{demagnetizing factor}$$

For non-spherical particles, N_d is largest along the small axis and smallest along the long axis. As a result, H_d is small along the long axis. Therefore, the magnetization prefers to align along the long axis. This anisotropy effect increases with the increase in the aspect ratio.

2.3.3 Stress anisotropy:

It becomes significant in materials having weak magnetocrystalline anisotropy, and polycrystalline materials which have no preferred orientation. It is a uniaxial anisotropy and the associated stress anisotropy energy, which is magnetoelastic energy, is given by:

$$E_{me} = K_\sigma sin^2\theta,$$

where K_σ= stress anisotropy constant

$$= \frac{3}{2}\lambda_{si}\sigma$$

(λ_{si} = isotropic magnetostriction constant)

For materials with positive K_σ, the axis of stress becomes easy axis whereas for materials with negative K_σ, the plane normal to the axis of stress becomes easy plane of magnetization.

It should be noted that stress alone can cause domain wall motion in demagnetized state.

2.3.4 Induced Magnetic Anisotropy:

Magnetic anisotropy can also be induced by some treatment like magnetic annealing, cold rolling, irradiation etc.

2.3.5 Exchange Anisotropy:

Exchange anisotropy was first discovered by Meiklejohn and Bean in 1956 while studying field-cooled, partially oxidised fine Co particles[4]. Exchange anisotropy leads to unidirectional anisotropy i.e. magnetization has only one stable positions instead of two as in the case of common uniaxial anisotropy. This anisotropy also leads to a shift in the

hysteresis loop, H_E, along the field axis on field cooling through the T_N of the AFM ($T_N < T_C$) in materials having ferromagnetic (FM)-antiferromagnetic (AFM) interfaces. This phenomenon is known as Exchange Bias. It has also been observed in other types of interfaces like AFM-ferrimagnetic[5] and FM-ferrimagnetic[6].

Hysteresis loop shift is also accompanied by an increase in coercivity, H_C below T_N. It is schematically represented in the figure 2.12[7].

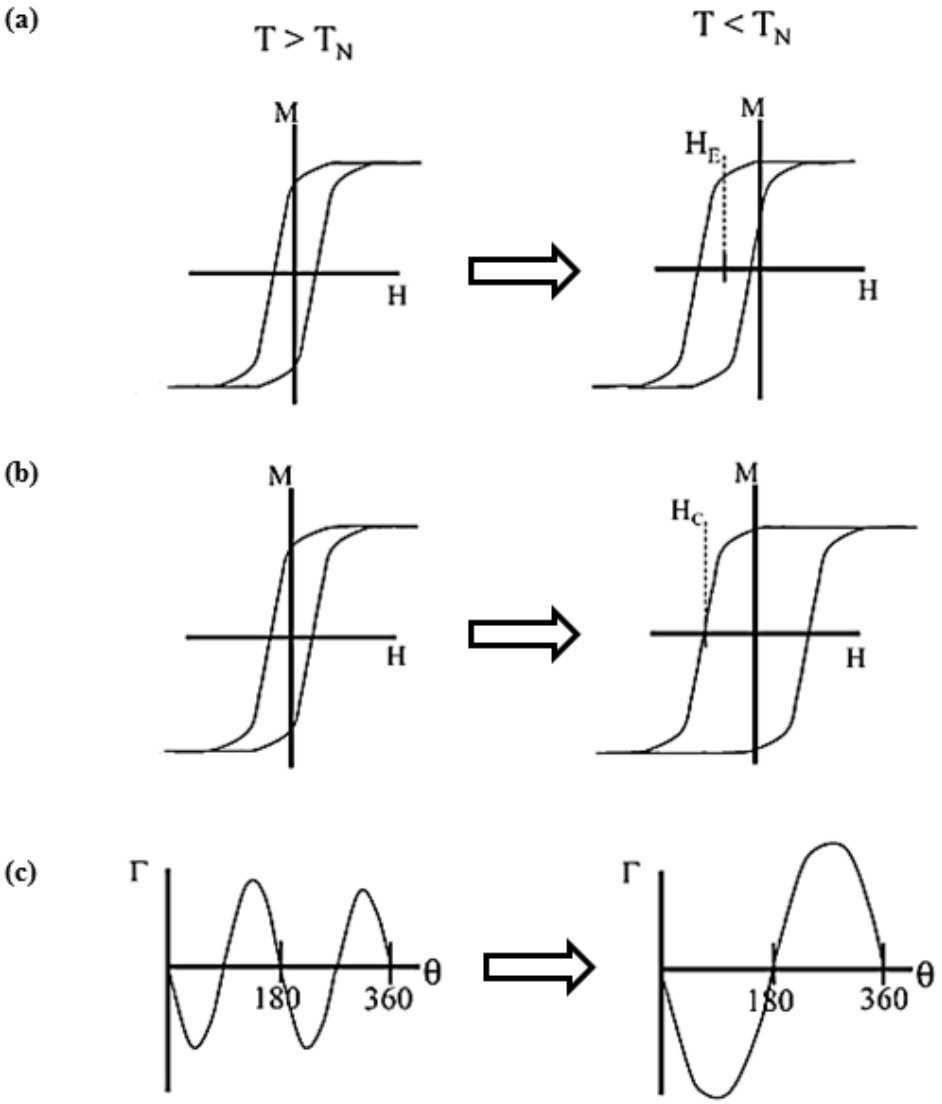

Fig 2.12 Schematic representation of (a) shift in hysteresis loop (b) increase in H_C and (c) unidirectional anisotropy, induced by FM-AFM exchange anisotropy (Reprinted with permission from [7].Copyright 2005 Elsevier B.V.)

2.4 Exchange Interactions:

2.4.1 Superexchange:

In 1934, Kramers first pointed out that it is possible to have an exchange spin-coupling between magnetic ions via an intermediate non-magnetic ion[8]. Later P. W. Anderson refined the Kramers' model in 1950[9].

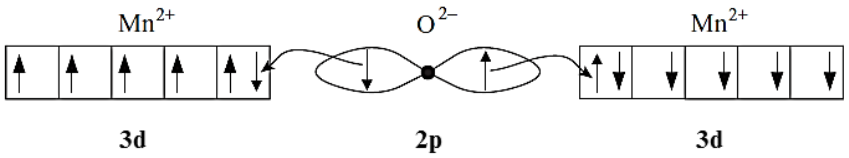

Fig 2.13 Schematic of superexchange mechanism in MnO

It can be best illustrated by taking MnO as an example. In MnO, Mn^{2+} ions ($3d^5$) are linked by O^{2-} ions to form Mn-O-Mn linear chains. The p-orbital of O^{2-}, therefore, is oriented along the Mn-O-Mn axis. Valence bonding between Mn^{2+} and O^{2-} ions can occur when O^{2-} donates an electron each to the two Mn^{2+} ions from its filled shell. This is possible only if the 3d electrons of one Mn^{2+} ions are spin-up and the other Mn^{2+} has electrons with spin-down. This leaves an overall antiferromagnetic alignment between the Mn^{2+} ions, thereby resulting to antiferromagnetic nature of MnO.

The strength and sign of superexchange can be predicted from a set of empirical rules known as Goodenough-Kanamori-Anderson rules[10] The rules are:

1. 180° superexchange interaction between half-filled orbitals is strong and antiferromagnetic.
2. 90° superexchange interaction between half-filled orbitals is ferromagnetic and rather weak.
3. Superexchange due to overlap between a half-filled and an empty orbital of different symmetry is ferromagnetic and relatively weak.

2.4.2 Double Exchange:

The theory of double exchange was first introduced by Zener[11]. This kind of interaction is observed in mixed-valence compounds such as $La_xCa_{1-x}MnO_3$.

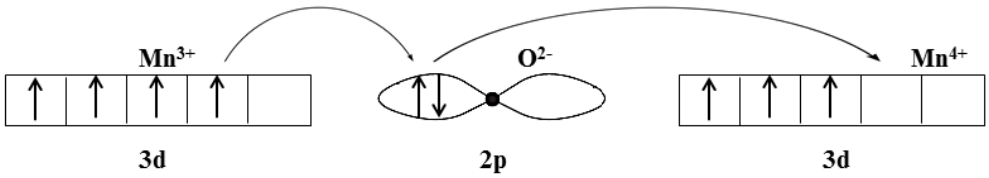

Fig 2.14 Schematic of double exchange mechanism

If we consider two Mn ions of different valence, say Mn^{3+} and Mn^{4+} bridged by O^{2-} ion, then there is a probability that an electron from Mn^{3+} can be transferred to Mn^{4+} via this bridging O^{2-}. Such an electron transfer is possible only when the magnetic moments of the two Mn ions are parallel to each other.

Double exchange mechanism accounts for the ferromagnetic nature of materials. Unlike superexchange interaction, it involves hoping of electrons from one metal ion centre to the other *via* non-magnetic ions and thus explains the anomaly of electrical conductivity in ferromagnetic phase. Double exchange in an antiferromagnetically ordered lattice leads to spin canting.

2.4.3 Dzyaloshinskii-Moriya interaction:

[12]Heisenberg exchange interaction between magnetic spin moments $\boldsymbol{S}$ located on atomic sites *i* and *j* is isotropic and symmetric and the energy associated is given by:

$$E_H = \sum_{i,j} J_{ij} \boldsymbol{S}_i . \boldsymbol{S}_j$$

where $\boldsymbol{S_i}$ and $\boldsymbol{S_j}$ are spin vectors and J_{ij} is the exchange constant. Depending on the value and the sign of J_{ij}, the interaction will be ferromagnetic or antiferromagnetic. In addition, there is magnetic anisotropy that is responsible for the occurrence of easy and hard axis. The energy associated is given by:

$$E_{ani} = \sum_i K_i sin^2 \varphi_i$$

where K_i is the anisotropy constant and φ_i is the angle between the axis of magnetization and the easy axis at site *i*. Magnetic anisotropy stabilizes magnetic ordering against thermal fluctuations.

However, due to the presence of spin-orbit coupling that connects the lattice with the spin symmetry, the lattice parity is broken and this gives rise to an additional interaction that breaks the inversion invariance of the Heisenberg Hamiltonian. This interaction is known as Dzyaloshinskii-Moriya (DM) interaction[13]. It is an antisymmetric and anisotropic exchange coupling between two spins (magnetic moments) on a lattice bond *ij* (with no inversion centre), induced by the relativistic spin-orbit coupling and has the form:

$$E_{DM} = \sum_{i,j} \boldsymbol{D}_{ij} . [\boldsymbol{S}_i \times \boldsymbol{S}_j]$$

where $\boldsymbol{D}_{ij}$ is known as Dzyaloshinskii-Moriya vector. Depending on the sign, the symmetry properties and the value of $\boldsymbol{D}_{ij}$, uniaxial ferromagnetic or antiferromagnetic structures fail to exist. Instead, a directional non-collinear magnetic structure of one specific chirality, $\boldsymbol{C}_i = \boldsymbol{S}_i \times \boldsymbol{S}_{i+1}$, either a right handed for $C>0$ or left handed for $C<0$ is formed.

DM interaction is responsible for canted antiferromagnetism or weak ferromagnetism.

2.4.4 RKKY interaction:

It was originally proposed by M.A. Ruderman and C. Kittel to explain the broad nuclear spin resonance line observed in metallic silver[14]. According to them, the magnetic moments of two nuclei can couple via their hyperfine interaction with the conduction electrons. Later T. Kasuya[15] and K.Yosida[16] extended this concept to the localized spins of atoms with a partially filled inner d-shell.

A magnetic ion can polarize the conduction electrons. These conduction electrons are delocalized and can transfer their polarization to other magnetic ions. RKKY interaction can be ferromagnetic or antiferromagnetic depending on the distance between the ions.

2.5 Exchange Bias:

Many models have been proposed to explain the phenomenon of exchange bias. The can be classified, according to Coehoorn[17], as macroscopic, mesoscopic[18] and microscopic[19] models depending on the lateral length scales. But it is still highly controversial. Yet it can be explained by a rather simple intuitive approach, as proposed by Meiklejohn and Bean[4, 20], based on the alignment of AFM spins at the interface of FM-AFM. This model assumes that the easy axes of FM and AFM are parallel and magnetization rotates coherently. According to this model[7], when a large magnetic field is applied at a temperature T such that $T_N < T < T_C$, the spins in the ferromagnetic layer are aligned along the field direction whereas the spins in the AFM layer are randomly oriented. On cooling through T_N, the spins in AFM layer begin to order antiferromagnetically. The spins at the interface of FM-AFM layer tend to interact with each other via exchange coupling and it would be expected that the first layer of spins in AFM layer prefers to align parallel to the ferromagnetic spins while the successive layers of spins will be aligned to give a net zero magnetization (figure 2.15(a)). Two different limiting cases can be considered:

1. Antiferromagnetic anisotropy is large
2. Antiferromagnetic anisotropy is small

2.5.1 when AFM anisotropy K_{AFM} is large:

On reversing the direction of applied field H, if the AFM anisotropy K_{AFM} is large, the spins in the AFM tend to align in the original direction and as spin interactions exist at the interface, they exert a microscopic torque on the spins in the FM layer. This torque resists the rotation of FM spins along the reverse field direction (figure 2.15(b)). As a result, a large magnetic field has to be applied to completely reverse the direction of FM spins (figure 2.15(c)).

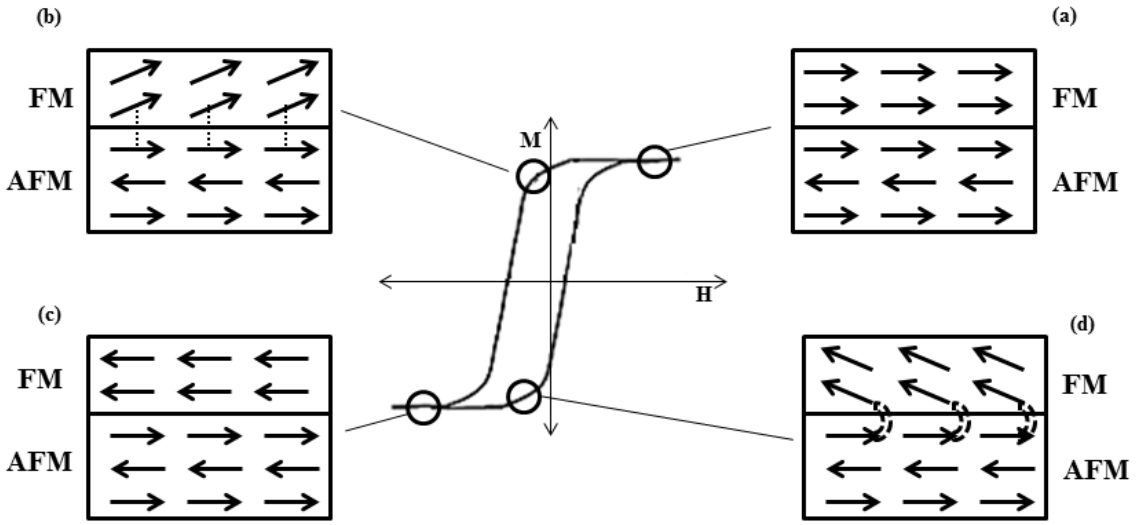

Fig. 2.15 Schematic diagram of spins in FM-AFM couple when K_{AFM} is large

If the magnetic field is then reversed back to positive value, the direction of the torque is along the field direction facilitating the reversal of magnetic moment thereby reducing H_C value in the positive field branch at the expense of small magnetic field (figure 2.15(d)). Therefore, there is a shift in the hysteresis loop along the magnetic field axis H_E. Moreover, due to this pinning effect by the spins in the FM-AFM interface, spins in the FM layer have only one stable configuration i.e. unidirectional anisotropy along the positive field direction.

2.5.2 when AFM anisotropy K_{AFM} is small:

In this case, when the magnetic field is applied in the reverse direction, the FM spins rotate along with AFM spins (figure 2.16(b)). But an extra energy is required for the rotation of AFM spins and this extra energy manifests as enhancement in H_c (figure 2.16(c)). Similar behaviour is observed on applying positive field after having saturated in the negative field. This leads to broadening of hysteresis loop.

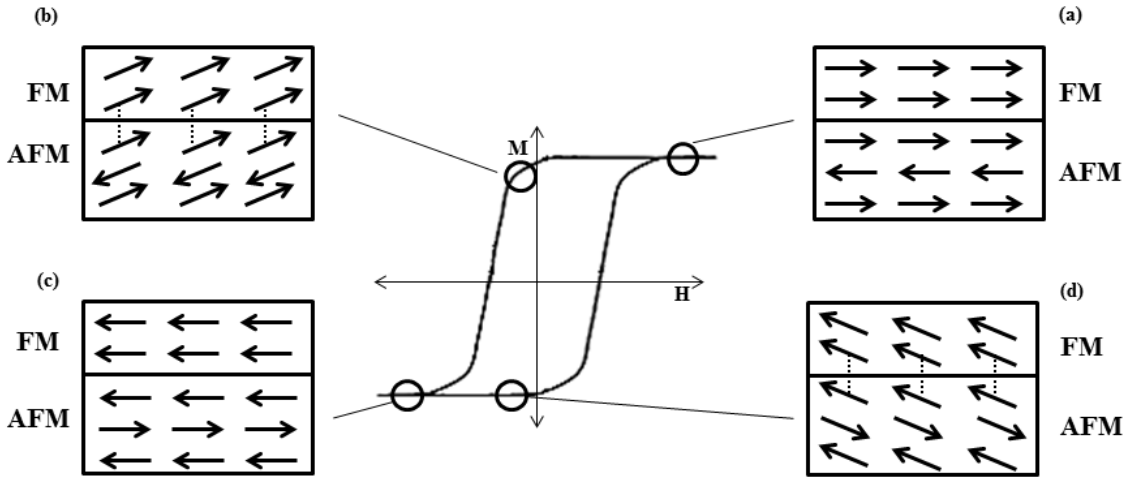

Fig. 2.16 Schematic diagram of spins in FM-AFM couple when K_{AFM} is small

This approach is valid only for thin films. But the values predicted for H_E, using this model, are usually much greater than the experimentally observed values. Therefore, Néel modified this model by bringing in the concept of a domain wall formation instead of a sharp FM-AFM interface[21]. This domain wall formation decreases the energy of the equilibrium magnetic configuration and hence the coupling between the FM-AFM spins. The values of H_E, thus, obtained is usually found to be much closer to experimentally observed values.

The temperature at which the exchange bias field becomes zero is known as blocking temperature (T_B).

For polycrystalline FM-AFM nanocomposite systems, we need to consider effects of grain formation. Stiles and McMichael[22] considered that AFM layer is constituted by an ensemble of crystallites which are of different sizes and different directions of easy axes. For a nanocomposite system, three cases can be considered[7]:

1. For the grains whose AFM easy axes is close to the field cooling direction, the AFM spins will resist to rotate on reversing the field and therefore, these crystallites contribute to loop shift.

2. For the grains whose AFM easy axes are oriented at an angle more than a critical angle to the field cooling direction, the AFM spins will rotate along with the FM spins on reversing the field. The AFM spins and FM spins should have a strong exchange coupling interaction. Therefore, these crystallites lead to enhancement in H_C.
3. For the grains in which the AFM-FM spin coupling is too weak, they do not have any contribution to exchange bias.

Both exchange bias H_E and H_C depend on the thickness of FM (t_{FM}) and AFM (t_{AFM}) layers. H_E and H_C are roughly inversely proportional to t_{FM}. H_E is independent of t_{AFM} for thick AFM layers but it decreases as t_{AFM} reduces and finally becomes zero for very small t_{AFM}[23]. And H_C increases with t_{AFM} until t_{AFM} reaches a critical value where it decreases to yield the value corresponding to the uncoupled FM[7].

The exchange biased systems is accompanied by a property known as *training effect*. There is reduction in H_E and H_C values on measuring consecutive hysteresis loops. This can be attributed to the reorientation of AFM domains with the reversal of FM magnetization each time as AFM spins try to find a more energetically favourable configuration[23].

As it is discussed above, usually the bias field is opposite to the field cooling. This is *normal exchange bias* (NEB). But sometimes the displacement of the loop is found to be in the same direction as the field cooling direction. This is known as *positive exchange bias* (PEB). It was first observed in FeF_2/Fe bilayer[24]. There have been many theoretical works put forward on the basis of antiferromagnetic FM-AFM interface exchange interaction[25]. But these theories are hard to justify physically. Recently Orlando V. Billoni *et. al.*[26] propose a mechanism based on domain wall formation. The interface of AFM-FM layers consists of disordered spins. These disordered spins form domain wall on field cooling and minimized the exchange energy due to frustration. This energy is stored at the interface through the Zeeman coupling of AFM spins. On reversing the magnetisation field, this energy is restored thereby producing a positive bias in the hysteresis loop.

Materials which show exchange bias can be used as "spin-valve" devices based on their *giant magnetoresistance* (GMR) (change in resistance on applying magnetic field) properties.

2.6 Spin Glass:

A spin glass magnetic system is a system with frustrated interactions among the highly disordered magnetic spins. There exists random competition between ferromagnetic and antiferromagnetic interactions thereby resulting to frustration. Frustration refers to conflicts between interactions that contradicts each other and cannot be obeyed simultaneously. In other words, frustration arises when spin pairs at sites *i* and *j* get different ordering instructions through various paths that link *i* and *j* either directly or via intermediate spins. In a triangle of three ising spins in which two bonds has $+J$ and the third has $-J$ as shown in figure 1.18, one spin always remains frustrated (with ground state degeneracy being six-fold).

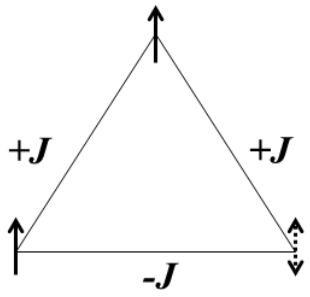

Fig. 2.18 Ising model of triangle lattice with frustrated interaction

The spins are frozen below a certain temperature known as freezing temperature T_f[27]. Above this temperature, it behaves as a normal ferromagnetic or antiferromagnetic. As T approaches T_f, the temperature induced-disorder is removed and various spin components begin to interact with each other over a long range. The system seeks its ground state *(T=0)* configuration for the particular distribution of spins and exchange interactions. Due to local anisotropy, the original random alignment of spins can be

locked into a preferred orientation and the system is trapped in a metastable configuration[28].

2.7 Superparamagnetism:

If the size of a particle is so small such that domain formation is not favourable, single domain particles are formed. Magnetization of such particles is determined by shape and magnetocrystalline anisotropies.

The magnetization of the particle lies along an easy direction in the absence of an external magnetic field. If a magnetic field is applied in the opposite direction, the magnetization has to rotate through the hard axis to orient along the field direction. The anisotropy energy is given by *KV*, where *K* is the anisotropy constant and *V* is the volume of the particle. As the particle size decreases, it becomes comparable to k_BT. As a result the thermal energy can overcome the anisotropy energy and the magnetization is no longer stable. It can reverse its direction from one easy axis to another even in the absence of a field. This phenomenon is known as *superparamagnetism.*

Superparamagnetic materials do not show any hysteresis. This behaviour is analogous to paramagnetic materials with the difference that rather than individual electronic spins, it is the collective moment of the particle and therefore, a much larger magnetic moment. Hence they are termed as superparamagnetic. The temperature at which a nanomaterial becomes superparamagnetic is called blocking temperature[29].

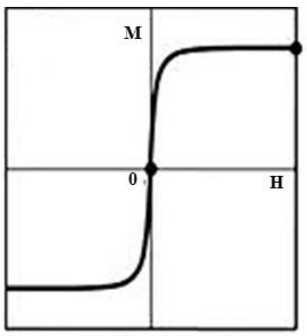

Fig. 2.19 Variation of magnetisation with magnetic field at $T < T_B$ for a superparamagnetic material

2.8 Neutron diffraction:

Neutron diffraction is an important tool to elucidate the magnetic spin structure of materials. Neutrons have wavelength in the order of 1 Å that is comparable to interplanar spacings in crystals. Neutrons offer various advantages over X-rays and electrons. They are neutral particles and therefore unlike X-rays and electrons, they are not scattered by electron density of the atoms. They can easily penetrate through the electron cloud and are scattered only by the nucleus. Moreover, they have a magnetic moment of its own of the order of $10^{-3}\mu_B$. Therefore, if the atoms or ions have a net magnetic moment due to their electrons, then neutron beams will interact with that moment as well. Hence, neutron scattering from a magnetic atom or ion has two parts, viz. nuclear part and magnetic part. In the case of electron beam, the electrostatic interaction with the electron cloud of the magnetic atom or ion is so strong that the magnetic interaction with the net magnetic moment of the electrons is not observable. However, these elementary magnetic moments can be seen in neutron diffraction and this makes neutron diffraction a very important tool for magnetic studies.

Neutron diffraction is governed by Bragg law that states that neutron beams which are scattered in the direction making an angle θ with the atomic planes equal to the angle of incidence will be in phase with each other and undergo constructive interference. In all other directions of space the phase relations between the scattered beams is such that they undergo destructive interference. The Bragg equation is of the form:

$$n\lambda = 2d\ sin\theta$$

where λ = wavelength of neutron

n = order of refelection

d = spacing of atomic planes in the crystal

θ = angle between the incident beam of neutrons and the atomic planes involved

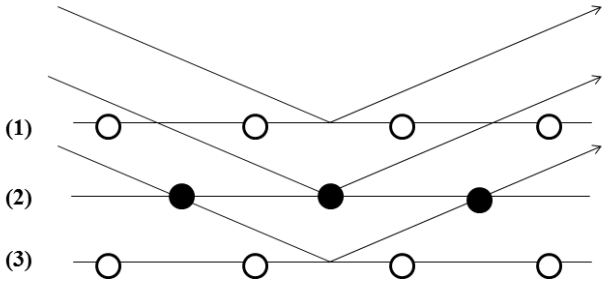

Fig.2.20 Diffraction in body centred cubic lattice

If a body-centred cubic lattice (b.c.c) is considered as shown in figure 2.20, planes (1) and (3) represent the (100) planes and plane (2) represents the plane that contains the body-centred atom. If the crystal is oriented such that the diffracted beams from planes (1) and (3) are in phase by Bragg condition, then the diffracted beam from plane (2) will be exactly out of phase with that from planes (1) and (3) thereby resulting to destructive interference and hence no (100) diffraction line will be observed. However if the material orders magnetically such that the orientation of magnetic moment in planes (1) and (3) is different from that of plane (2), then this will result to different scattering amplitude of the plane (2) from planes (1) and (3). Therefore, the (100) line will be observed in the diffraction pattern. It can, thus, be concluded that additional lines will appear in the neutron diffraction pattern on cooling an antiferromagnet through its Néel temperature as can be seen from the neutron diffraction pattern of MnO (figure 2.22).

MnO has the face-centred cubic rock structure as shown in figure 2.21(a). It orders antiferromagnetically with T_N = 120 K[30]. Below T_N, the unit size doubles and many more lines appear in the neutron diffraction pattern as shown in the lower panel of figure 2.22.

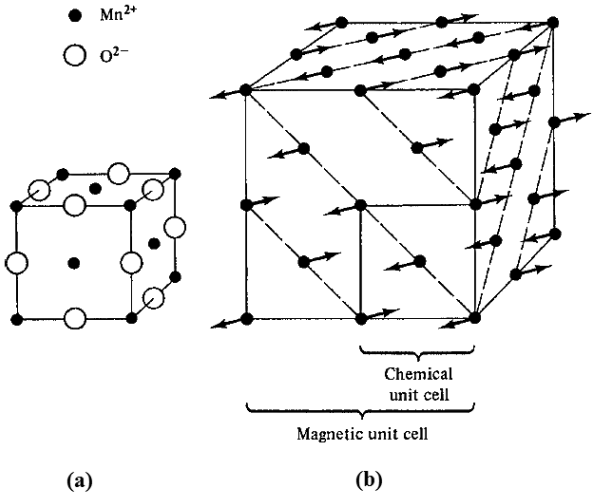

Fig. 2.21 Structure of MnO (a) chemical unit cell (b) magnetic unit cell (O ions are omitted for clarity (taken from [31])

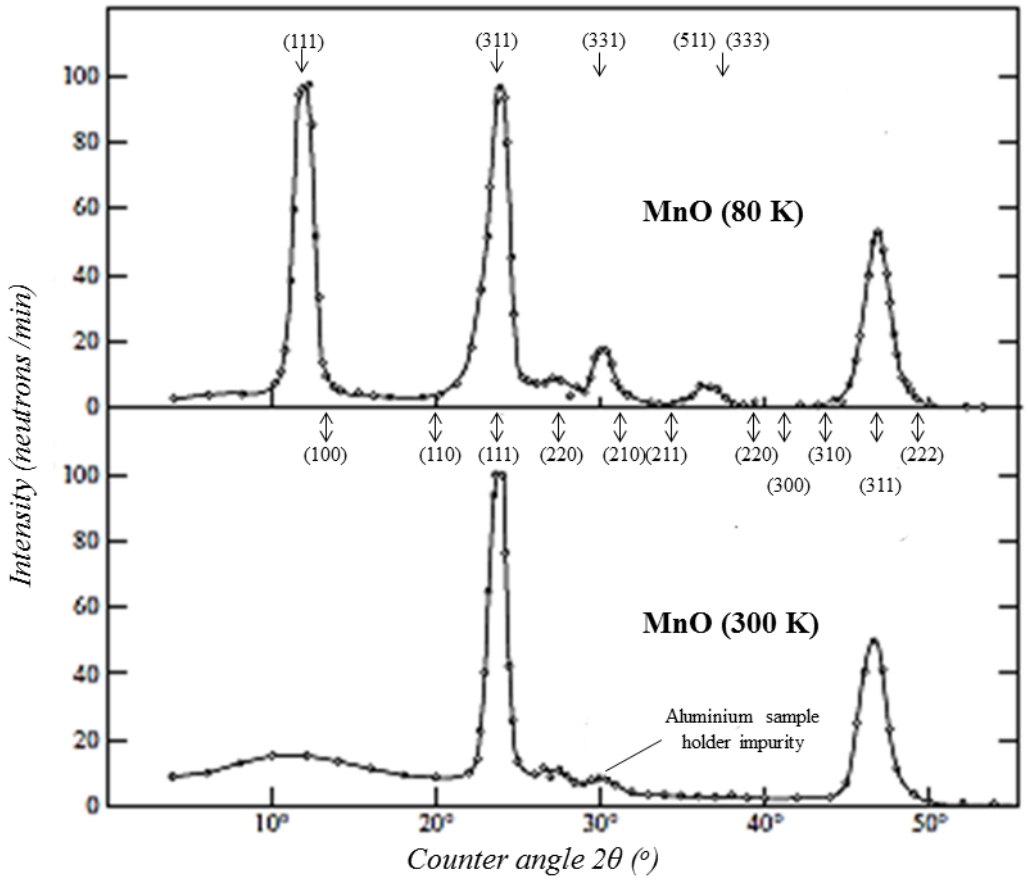

Fig 2.22 Neutron diffraction pattern of MnO at 80 K and 300 K (taken from [2])

1.8 References:

[1] E. C. Stoner, E. P. Wohlfarth, *Phil. Trans. R. Soc. London A* **1948**, *240*

[2] N. A. Spaldin, *Magnetic Materials - Fundamentals and Applications*, Second ed., Cambridge University Press, **2011**.

[3] L. Néel, *Ann. Phys.* **1948**, *3*.

[4] W. H. Meiklejohn, C. P. Bean, *Phys. Rev.* **1956**, *102*, 1413-1414.

[5] P. J. v. d. Zaag, R. M. Wolf, A. R. Ball, C. Bordel, L. F. Feiner, R. Jungblut, *J. Magn. Magn. Mater.* **1995**, *148*

[6] W. C. Cain, M. H. Kryder, *J. Appl. Phys.* . **1990**, *67*.

[7] J. Nogués, J. Sort, V. Langlais, V. Skumryev, S. Suriñach, J. S. Muñoz, M. D. Baró, *Phys. Rep.* **2005**, *422*, 65 – 117.

[8] H. A. Kramers, *Physica A* **1934**, *1*, 182-192.

[9] P. W. Anderson, *Phys. Rev. 1950* **1950**, *79* 350-356.

[10] (a) J. B. Goodenough, *Phys. Rev. 1955,100, 564* **1955**, *100*; (b) J. Kanamori, *J. Phys. Chem. Solid* **1959**, *10*; (c) P. W. Anderson, *Magnetism*, Academic Press, New York, **1963**; (d) J. B. Goodenough, *Magnetism and the Chemical Bond* Interscience Publisher, New York, **1963**.

[11] C. Zener, *Phys. Rev.* **1951**, *82*.

[12] M. Bode, M. Heide, K. von Bergmann, P. Ferriani, S. Heinze, G. Bihlmayer, A. Kubetzka, O. Pietzsch, S. Blugel, R. Wiesendanger, *Nature* **2007**, *447*, 190-193.

[13] (a) I. E. Dzyaloshinskii, *J. Phys. Chem. Solids* **1958**, *4*; (b) T. Moriya, *Phys. Rev.* **1960**, *120*, 91-98.

[14] M. A. Ruderman, C. Kittel, *Phys. Rev.* **1954**, *96*, 99-102.

[15] T. Kasuya, *Prog. Theor. Phys.* **1956**, *16*.

[16] K. Yosida, *Phys. Rev.* **1957**, *106*, 893-898.

[17] R. Coehoorn, *Handbook of Magnetic Materials, Vol. 15*, North-Holland, Amterdam, **2003**.

[18] (a) J. S. Kouvel, *J. Phys. Chem. Sol.* **1963**, *24* ; (b) E. Fulcomer, S. H. Charap, *J. Appl. Phys.* **(1972**, *43*; (c) T. Mewes, R. L. Stamps, *Appl. Phys. Lett.* **2004**, *84*; (d) J. Geshev, L. G. Pereira, J. E. Schmidt, L. C. C. M. Nagamine, E. B. Saitovitch, F. Pelegrini, *Phys. Rev. B* **2003**, *67* ; (e) J. Geshev, L. G. Pereira, J. E. Schmidt, *Phys. Rev. B* **2002**, *66* ; (f) D. Suess, M. Kirschner, T. Schrefl, W. Scholz, R. Dittrich, H. Forster, J. Fidler, *J. Appl. Phys.* **2003**, *93* ; (g) C. Hou, H. Fujiwara, K. Zhang, A. Tanaka, Y. Shimizu, *Phys. Rev. B* **2001**, *63*.

[19] (a) C. Mitsumata, A. Skuma, K. Fukamichi, *Phys. Rev. B* **2003**, *68*; (b) D. Suess, K. Krishner, T. Schrefl, J. Fidler, R. L. Stamps, J. V. Kim, *Phys. Rev. B* **2003**, *67*; (c) T. Mewes, B. Hillebrands, R. L. Stamps, *Phys. Rev. B* **2003**, *68*

[20] W. H. Meiklejohn, *J. Appl. Phys.* **1962**, *33*

[21] (a) L. Néel, *Ann. Phys. (France)* **1967**, *1*; (b) L. Néel, *C.R. Acad. Sci. Paris Serie C* **1967**, *264*

[22] M. D. Stiles, R. D. McMichael, *Phys. Rev. B* **1999**, *59*.

[23] J. Nogués, I. K. Schuller, *J. Magn. Magn. Mater.* **1999**, *192*, 203-232.

[24] J. Nogués, D. Lederman, T. J. Moran, I. K. Schuller, *Phys.Rev. Lett.* **1996**, *76*

[25] (a) N. C. Koon, *Phys. Rev. Lett.* **1997**, *78*; (b) T. C. Schulthess, W. H. Butler, *Phys. Rev. Lett.* **1998**, *81*; (c) M. Kiwi, J.Mejía-López, R. D. Portugal, R.Ramírez, *Europhys. Lett.* **1999**, *48*; (d) M. Kiwi, J.Mejía-López, R. D. Portugal, R.Ramírez, *Appl. Phys. Lett.* **1999**, *75*; (e) M. Kiwi, J.Mejía-López, R. D.

Portugal, R.Ramírez, *Solid State Commun.* **2000**, *116*, 315 ; (f) U. Nowak, K. D. Usadel, J. Keller, P. Miltényi, B. Beschoten, G. G¨untherodt, *Phys. Rev. B* **2002**, *66*; (g) Y. Hu, A. Du, *Phys. Status Solidi B* **2011**, *248*, 2932

[26] Billoni, Tamarit, Cannas, *Phys. Rev. B* **2013**, *88*, 020405(R).

[27] J. A. Maydosh, *J. Magn. Magn. Mater.* **1996**, *157/158*.

[28] F. Duan, J. Guojun, *Introduction to Condensed Matter Physics Vol. 1*, World Scientific Publishing Co. Pte. Ltd., Singapore, **2005**.

[29] (a) L. Néel, *C. R. Acad. Sci.* **1949**, *228*; (b) C. P. Bean, *J. Appl. Phys.* **1955**, *26*.

[30] C. G. Shull, W. A. Strauber, E. O. Wollan, *Phys. Rev.* **1951**, *83*, 333-345.

[31] B. D. Cullity, C. D. Graham, *Introduction to Magnetic Materials*, Second ed., Wiley-IEEE press, **2009**.

CHAPTER 3

Effect of Anion Substitution on the Magnetic Properties of Chromium (III) Oxide

Abstract:

Chromium (III) oxide is a well-known antiferromagnet with magnetic ordering temperature T_N = 308 K for bulk material. Substitution of oxygen in Cr_2O_3 with less electronegative nitrogen and more electronegative fluorine may induce local interactions in the system leading to distortion in local distances. Substitution of O with F or N alone induces a slight non-linearity in the *(M-H)* curve of the system. With co-substitution of O with equal concentration of N and F as well, there exists a slight non-linearity in the *(M-H)* curve. However, on co-doping Cr_2O_3 with nitrogen and fluorine with excess amount of N, a marked difference in the magnetic properties was observed. It shows a huge divergence of FC and ZFC magnetization curves. The antiferromagnetic transition temperature was not identifiable. Moreover, a weak ferromagnetism was observed and the hysteresis loop shifts along the vertical axis on cooling in presence of an external field. There is a slight increase in the coercivity on increasing strength of the cooling field. The observed behaviour of the system may be attributed to the defects introduced in the system due to unequal proportions of nitrogen and fluorine.

3.1 Introduction:

It is customary to carry out substitution of cations in inorganic solids such as metal oxides to bring about changes in the structural property. There are numerous examples of such substitution of cations in oxides having carried out with great effectiveness. Substitution of oxygen in oxides by anions would also be expected to bring about changes in the structures and properties of the material. There are few reports where oxide ion is substituted by nitrogen[1] and fluoride[2] ions. Doping with fluorine will have negligible effect on electronic properties of O^{2-} ions as the p-orbitals of fluorine are lower in energy than those of the less electronegative oxygen atoms. In contrast, substitution of oxygen by less electronegative nitrogen is expected to produce significant changes to magnetic properties of the material. However, substitution with N^{3-} ions leads to anion vacancy so as to neutralise the charge of the crystal. It should be noted that two O^{2-} ions are isoelectronic with one N^{3-} and one F^{-} ion together. Co-substitution of O^{2-} by both N^{3-} and F^{-} is therefore desirable to bring about major changes in electronic properties without causing defects in the crystal[3]. Recently N, F substitution in ZnO and TiO_2 has been studied. ZnO when co-substituted with N and F to a moderate strength has reduced band gap compared to undoped ZnO and therefore change in colour from white to bright orange has been observed[3b]. TiO_2 substituted with N, F behaves similarly. On doping with N and F, TiO_2 changes its colour from white to yellow[4]. Rao et. al. has also studied the magnetic properties of N, F- doped TiO_2 nanoparticles[4]. Elfimov et. al.[1a] had shown that substitution of O with N in simple nonmagnetic oxides, like SrO, leads to holes in N 2*p* states which form local magnetic moments. They have predicted these materials to be ferromagnetic metals or small band gap insulators because of the very large Hund's rule coupling between the N and O 2*p*.

Substitution of N and F in oxides also results in local interactions involving relatively positive nitrogen and relatively negative fluorine causing changes in local distance. We, therefore, have investigated the effect of nitrogen and fluorine substitution on magnetism of Cr_2O_3.

Bulk Cr_2O_3 is a well-known antiferromagnet with antiferromagnetic ordering temperature T_N = 308 K[5]. It crystallizes in the corundum structure (space group $R\bar{3}c$) as shown in figure 3.1(a).

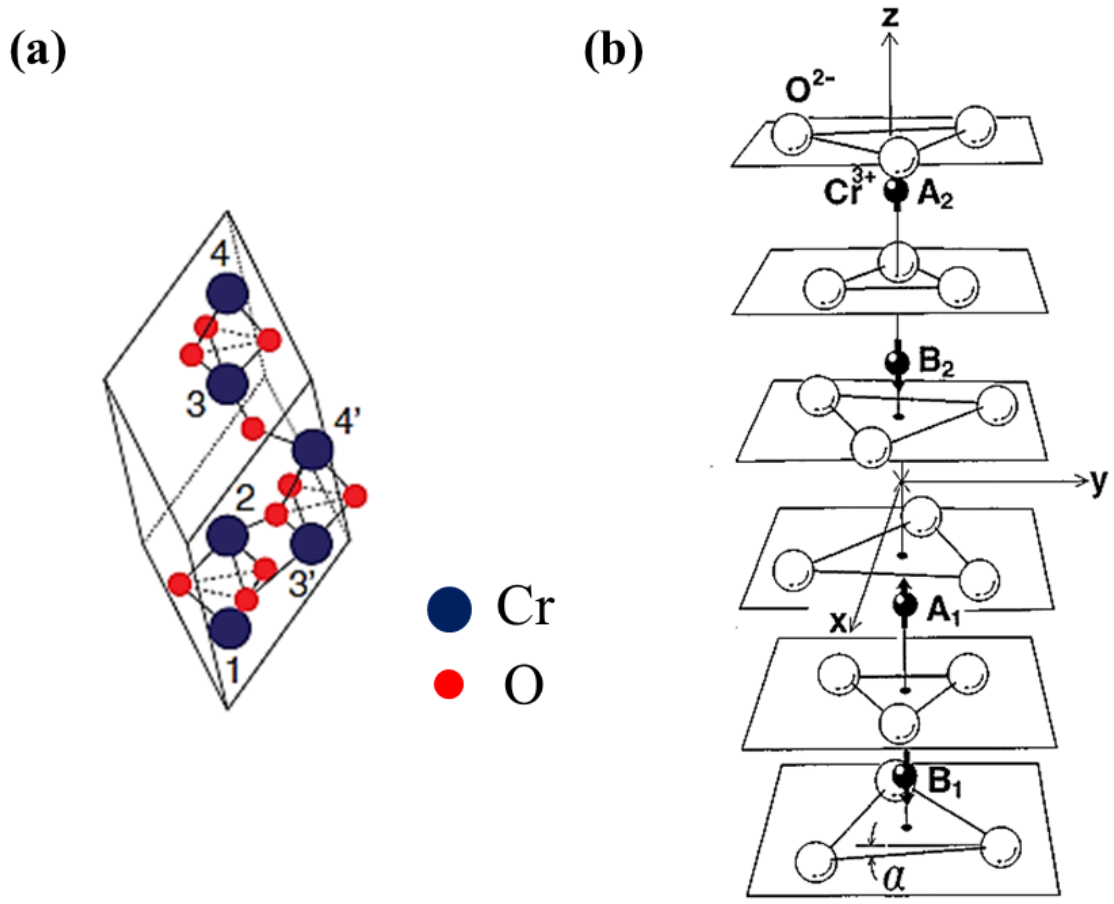

Fig 3.1 (a) Crystal structure (Reprinted with permission from [6]. Copyright 2013 The Japan Society of Applied Physics) and (b)Antiferromagnetic structure of Cr_2O_3 (Reprinted with permission from [7]. Copyright 1998 The American Physical Society)

Below T_N, the crystal loses both the inversion and time-reversal symmetry and adopts the symmetry $R\bar{3}'c'$ [7]. The unit cell of Cr_2O_3 consists of four Cr^{3+} ions, each surrounded by six O^{2-} ions. The *z* axis is taken along the three-fold (C_3) axis of the crystal whereas the *x* axis is taken along the two-fold (C_2) axis so that the *yz* plane becomes the mirror plane. Figure 3.1(b) shows the antiferromagnetic structure of Cr_2O_3. The origin of the co-ordinate axes is the inversion centre.

3.2 Scope of Investigation:

We have doped Cr_2O_3 with nitrogen and fluorine. We have done co-substitution of O with N and F as well. We have investigated the effect of substitution of O with the less electronegative N and more electronegative F on the magnetic properties of Cr_2O_3, which is otherwise antiferromagnetic.

3.3. Experimental Section:

3.3.1 Synthesis:

(a) Cr_2O_3 nanoparticles: 20 g of $Cr(OH)_3.9H_2O$ (Sigma Aldrich, $\geq$ 98.0 % pure, ACS grade) was added to approximately 200 mL of deionised water in a 500 mL beaker and was kept for stirring at 60^{o}C till it dissolves completely. Once the dissolution is over, solution of anhydrous citric acid (20 g) (Sigma Aldrich, $\geq$ 99.5 % pure, ACS grade) in 100 mL deionised water was added slowly with continuous stirring. Approximately 100 mL of deionised water was further added and was kept for stirring for nearly 15 min at 60^{o}C. The temperature was then increased to 90^{o}C and kept overnight. Gel was formed after the solvent had completely evaporated. At that stage, the beaker was transferred to an oven whose temperature was maintained at 180^{o}C. After approximately 5 hr, it was then cooled to room temperature and ground by using mortar-pestle. It was finally decomposed by heating at 700^{o}C for 2 hr in air to give Cr_2O_3 nanoparticles. The as-prepared Cr_2O_3 was later annealed at 700^{o}C for 4 hr in air.

a) F-doped Cr_2O_3: Cr_2O_3 nanoparticles and ammonium fluoride (Spectrochem, 99% puriss AR) were taken in molar ratio 1:30 and was ground together thoroughly by using mortar pestle. The mixture was heated in air at 700^{o}C for 4 hr to give F-doped Cr_2O_3.

b) N-doped Cr_2O_3: Cr_2O_3 nanoparticles was heated at 600^{o}C for 4 hr under the continuous flow of NH_3 gas to give N-doped Cr_2O_3.

c) **N, F-co-doped Cr_2O_3:** Cr_2O_3 nanoparticles and ammonium fluoride were taken in the molar ratio of 1:20 and were ground together by using mortar pestle. It was then heated at 600^{o}C for 8 hr under the continuous flow of NH_3 gas to give N, F-co-doped Cr_2O_3. This reaction was also carried out with the same molar ratio of the starting materials but heated at different temperature and duration (700^{o}C for 4 hr) under the continuous flow of NH_3 to obtain N, F-co-doped Cr_2O_3.

3.3.2. Characterization:

The phase purity of the samples obtained above was confirmed from powder X-ray diffraction (XRD) patterns which were recorded in PANalytical Empyrean monchromatic diffractometer (CuKα_1 radiation as source). The X-ray diffraction patterns were analysed by using a software package FullProf. It was found that all the synthesized samples crystallize in rhombohedral structure (Space group $R\bar{3}c$).

Morphology of the samples was determined by Field Emission Scanning Electron Microscopy (FESEM). From FESEM images, size as well as the size distribution of the particles was also obtained.

The percentage composition of the dopants (N and F) in the samples was determined from X-ray photoelectron spectra (XPS) which were recorded in Omicron nanotechnology ESCA (Model-EAC2000 SPHERA 547) (source-Mg Kα). Information on the bonding nature of the elements can be obtained by analysing the XPS of the samples. The XPS background subtraction was carried out by using an iterative procedure "Shirley algorithm". The XPS peaks after the background subtraction was fitted by using Voigt peak function.

UV-visible absorption spectra of these samples were recorded in Perkin Elmer lambda 750 in the percentage reflectance mode to verify if the doping of N and F has produced any significant changes in the band gap of the material. Raman spectra were also recorded for these samples using green LASER (532 nm). It was to verify if any changes in the local symmetry of the crystal is introduced with N and F substitution.

DC magnetization was measured in Superconducting Quantum Interference Device that employs Vibrating Sample Magnetometers (SQUID VSM) (Quantum Design, Magnetic Property Measurement System MPMS 3). Magnetization measurements were done under field-cooled (FC) and zero-field-cooled (ZFC) conditions in the temperature range of 2 to 390 K in the presence of a magnetic field of strength 100 Oe and 1000 Oe. Magnetic hysteresis loops were recorded at 2 K, 300 K and 390 K with the applied field ranging from -5 kOe to +5 kOe. Field-dependent hysteresis loop measurement were done by applying magnetic field of strength 5 T, 3 T, 1 T, -1 T, -3 T and -5 T with the temperature maintained at 2 K. Temperature-dependent magnetic hysteresis loop studies were carried out in the temperature range of 2 to 390 K in the presence of 1 T magnetic field.

3.4 Results and Discussion:

3.4.1 XPS Analysis:

The atomic percentage composition of an element 'a' (C_a) can be determined by using the following formula:

$$C_a = \frac{I_a/S_a}{\sum_{a,b,c\ldots} I/S} \times 100\%$$

where I_a – area under the peak corresponding to an inner orbital of element 'a'

S_a – atomic sensitivity factor of that orbital of the element 'a'

In our analysis to compute the N and F content of the sample, we have considered only those XPS peaks which correspond to N and F which are bonded to Cr^{3+}.

Figure 3.2(a) shows the XPS of F-doped Cr_2O_3.The signal at 687.39 eV confirms the presence of F in the sample. The F content of the sample was found to be 11.2 *at.* %.

The XPS of N-doped Cr_2O_3 shows a peak at B.E. = 397.84 eV (figure 3.2 (b)). This B.E. value is close to 396.4 eV which is the B.E. of N 1s peak for CrN[8]. In Cr_2O_3,

Cr^{3+}, to which N^{3-} is expected to be bonded, is linked to O^{2-} ions which are more electronegative than the N^{3-} ions. It is therefore expected that the displacement of electrons from Cr^{3+} towards N^{3-} ion is considerably reduced in the case of N-doped Cr_2O_3. As a result, the binding energy of 1s electron of N atom in N-doped Cr_2O_3 is increased to 397.84 eV. The N content of this sample 2 was found to be 5.4 *at.* %.

The XPS of another N-doped Cr_2O_3 (synthesized under similar conditions as the previous N-doped sample) shows a peak with shoulder (figure 3.2 (c)) which can be deconvoluted into two peaks *viz.* at 396.74 eV and 398.77 eV. The B.E. value of 396.74 eV is close to that of N 1s in CrN. This confirms the presence of N bonded to Cr^{3+} in the sample. The peak at 398.77 eV corresponds to N 1s of (N-H) groups[9]. The N-content of this sample was found to be 6.2 *at.* %.

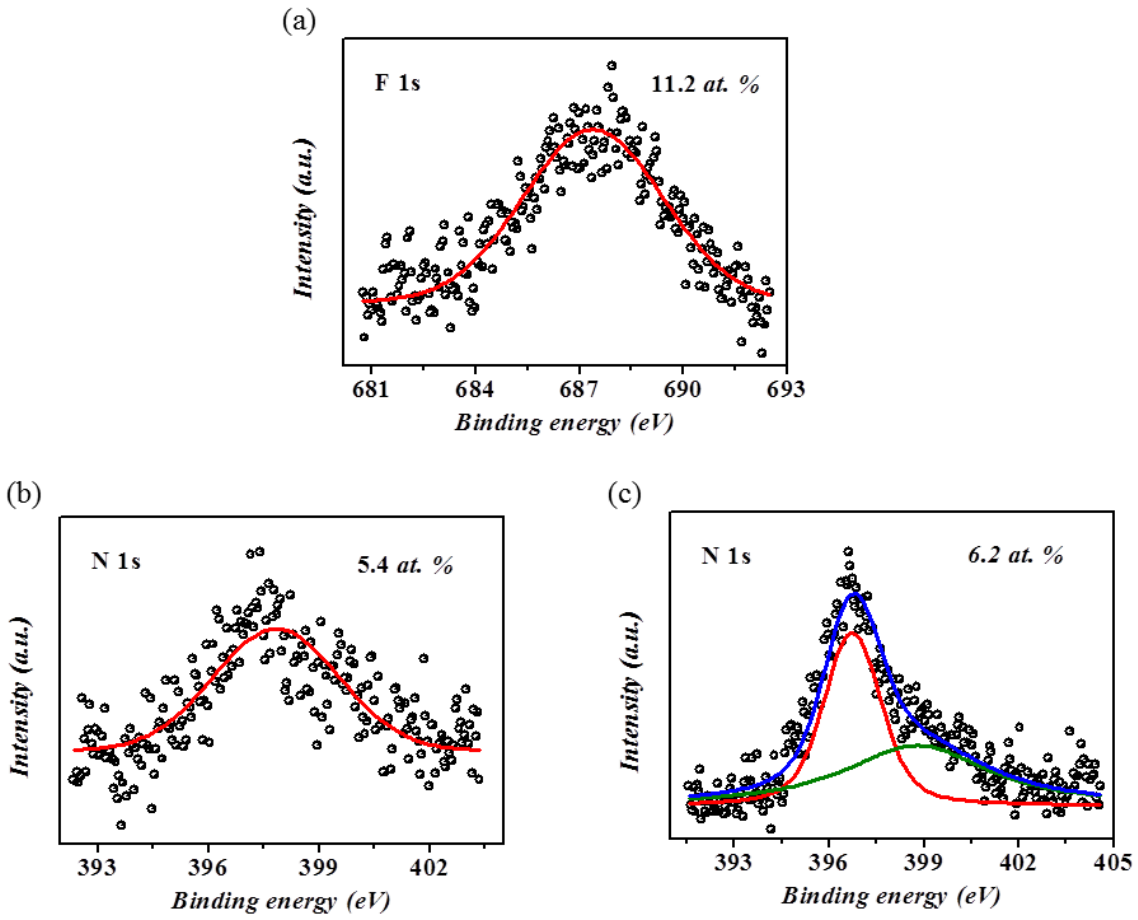

Fig 3.2 XPS of (a) F-doped Cr_2O_3 and (b) and (c) N-doped Cr_2O_3

The XPS of N, F-co-doped Cr_2O_3 (synthesized at 600°C/8 hr, NH_3 atmosphere) shows a peak with shoulder in the region 393 eV to 403 eV as can be seen from figure 3.3(a). This peak was deconvoluted into 2 peaks *viz.* at B.E. 395.94 eV and 399.20 eV. The peak at 395.94 eV corresponds to the B.E. of 1s electron in N bonded to Cr^{3+} whereas the peak at 399.20 eV corresponds to the B.E. of 1s electron in N of (N-H) group[10]. The inset of figure 3.4(a) shows the XPS of sample 4 in the region 678 eV to 693 eV. A peak appears at 685.10 eV and this corresponds to the B.E. of 1s electron of F bonded to Cr^{3+} ion[11]. The N and F content of the sample were found to be 8.1 and 7.3 *at.*% respectively.

The XPS of another N, F-co-doped Cr_2O_3 (synthesized at 700°C/4 hr, NH_3 atmosphere) is shown in figure 3.3(b). A peak appeared at B.E. value of 396.09 eV which corresponds to 1s electron of N bonded to Cr^{3+}. The inset of figure 3.4(b) shows the XPS of F 1s whose B.E. is 685.10 eV. The N and F content of the sample were found to be 5.1 *at.* % each.

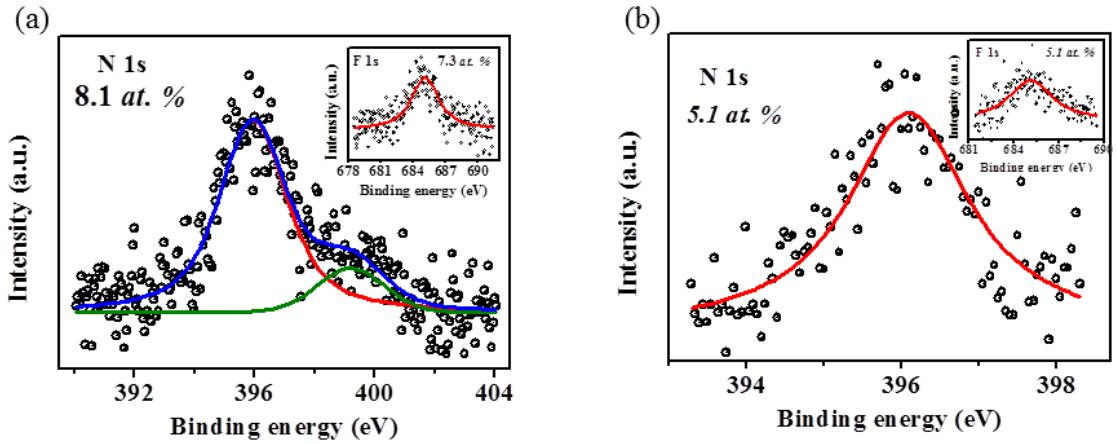

Fig. 3.3 XPS of N, F-co-doped Cr_2O_3 samples prepared at different reaction conditions

The XPS of third N, F-co-doped Cr_2O_3 ((synthesized at 600°C/8 hr, NH_3 atmosphere) shows a peak at 396.40 eV that corresponds to 1s electron of N bonded to Cr^{3+} (figure 3.4). The peak at 685.4 eV (inset of figure 3.4) is due to 1s electron of F. The N and F content of this sample were found to be 8.8 and 5.9 *at.* % respectively.

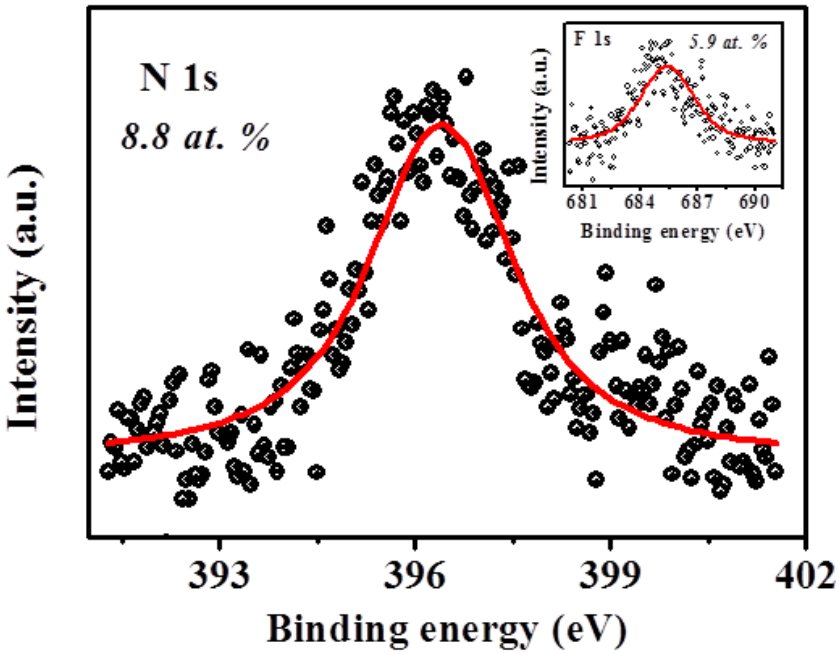

Fig. 3.4 XPS of N, F-co-doped Cr_2O_3 (sample 6)

3.4.2 Analysis of X-Ray Diffraction patterns:

Powder X-ray diffraction (XRD) pattern of as-prepared Cr_2O_3 shows that it crystallises in corundum structure (space group $R\bar{3}c$) (figure 3.5 (a)). The phase purity of the sample was confirmed by profile fitting of the powder XRD pattern by Le Bail method using fullprof software package (figure 3.6(a)). The lattice parameters were obtained as a = 4.9580(2) Å and c = 13.6011(6) Å. The average crystallite size of the crystals is computed from XRD data by using the Scherrer equation:

$$D = \frac{K\lambda}{B\cos\theta}$$

where K – Scherrer constant (= 0.89 for spherical particle)

D – diameter of the particle

λ – wavelength of X-ray (= 1.54056 Å for Cu $K\alpha_1$)

B – full width half maxima (FWHM) of the XRD peak

θ – Bragg angle of the XRD peak

The (012) diffraction peak of Cr_2O_3 was fitted with voigt peak function and considering the FWHM and the Bragg angle θ for this peak, the crystallite size was calculated and was found to be 21 nm.

Crytallinity of Cr_2O_3 was improved by annealing as it is evident from sharp Bragg peaks in the XRD pattern (figure 3.5(b)). The phase purity of the annealed sample was confirmed from the profile fitting of XRD pattern (figure 3.6 (b)). Lattice parameters of the annealed sample were a = 4.9594(1) Å and c = 13.5959(2) Å. Scherrer equation gives the crystallite size as 103 nm.

N-doped, F-doped and N, F-co-doped Cr_2O_3 samples were also found to crystallise in corundum structure (space group $R\bar{3}c$) similar to undoped Cr_2O_3 (figure 3.5(c)-(h)). On fitting the XRD profiles by Le Bail method, the lattice parameters of these doped samples were found to differ slightly from the undoped sample. Lattice parameters of N-doped as well as N, F-co-doped samples increase slightly (a = 4.9606(6) Å and c = 13.6058(18) Å for 6.2 *at.* % N-doped Cr_2O_3 and a = 4.9597(4) Å and c = 13.6055(15) Å for 8.8 *at.*% N, 5.9 *at.* % F-co-doped Cr_2O_3). Lattice parameter a = 4.9587(4) Å of F-doped sample was close to that of as-prepared Cr_2O_3 as well as the annealed Cr_2O_3. However, lattice parameter c = 13.5988(13) Å decreases slightly compared to that of as-prepared sample but increases slightly compared to that of annealed Cr_2O_3.

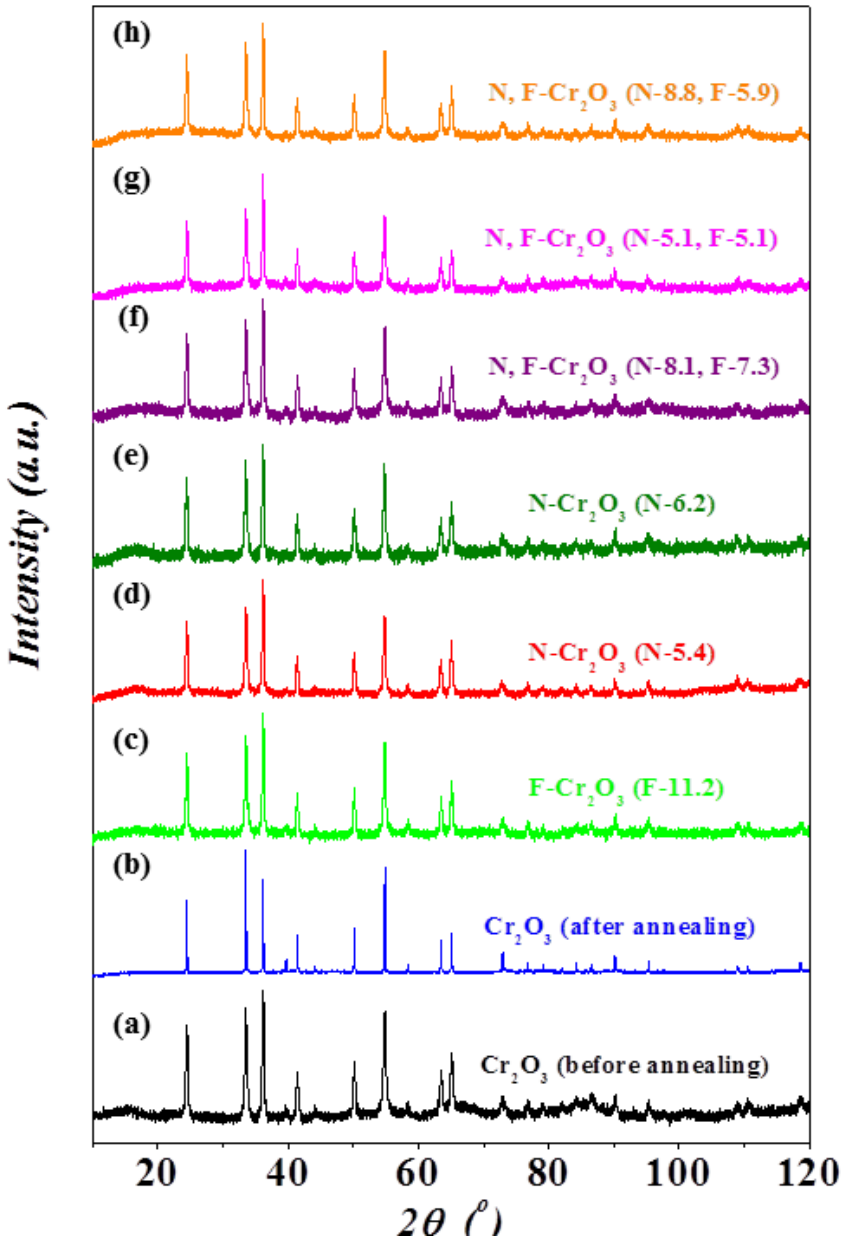

Fig. 3.5 Powder X-Ray Diffraction patterns of (a) Cr_2O_3 (as-prepared) (b) Cr_2O_3 (after annealing) (c)F-doped Cr_2O_3 (F-11.2) (d) N-doped Cr_2O_3 (N-5.4) (e) N-doped Cr_2O_3 (N-6.2) (f) N, F-co-doped Cr_2O_3 (N-8.1, F-7.3) (g) N, F-co-doped Cr_2O_3 (N-5.1, F-5.1) (h) N, F-co-doped Cr_2O_3 (N-8.8, F-5.9)

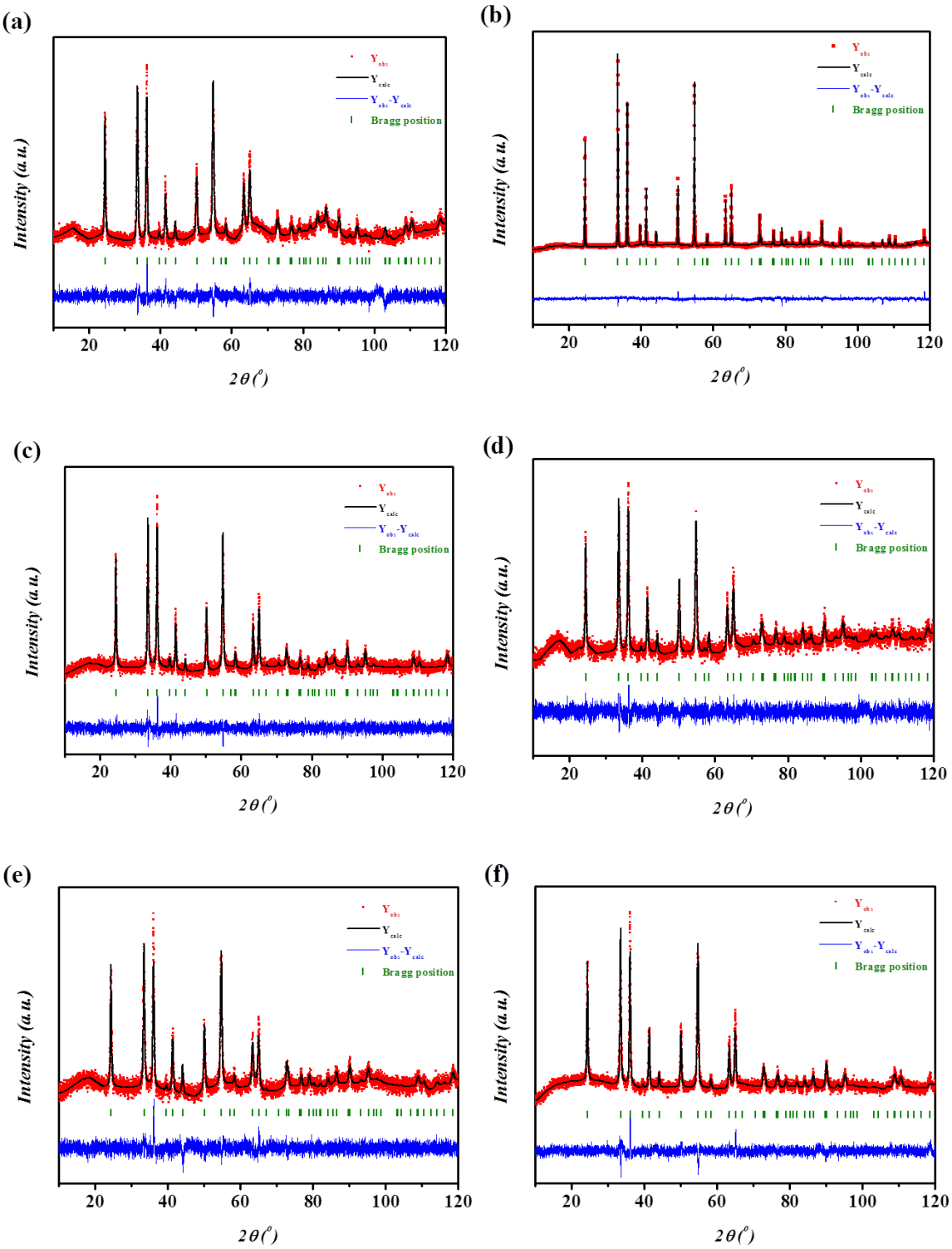

Fig. 3.6 Powder X-Ray Diffraction patterns with profile fits, difference patterns and Bragg positions of (a) Cr_2O_3 (as-prepared) (b) Cr_2O_3 (after annealing) (c) F-doped Cr_2O_3 (F-11.2) (d)N-doped Cr_2O_3 (N-6.2) (e)N, F-co-doped Cr_2O_3 (N-8.1, F-7.3) (f) N, F-co-doped Cr_2O_3 (N-8.8, F-5.9)

The crystallite size of the other samples was also calculated from Scherrer equation and was found to be in the range of 20 nm – 25 nm. The lattice parameters and the average crystallite size of all the samples are listed in table 3.1.

Table 3.1 Lattice parameters and crystallite size of Cr_2O_3 and doped Cr_2O_3 samples

Sample	Space Group: $R\bar{3}c$ Lattice parameters		Crystallite size (nm)
	a (Å)	*b* (Å)	
Cr_2O_3 *(before annealing)*	4.9580(2)	13.6011(6)	21
Cr_2O_3 *(after annealing)*	4.9594(1)	13.5959(2)	103
F-doped Cr_2O_3 *(F-11.2 at. %)*	4.9587(4)	13.5988(13)	24
N-doped Cr_2O_3 *(N-6.2 at. %)*	4.9606(6)	13.6058(18)	22
N, F-co-doped Cr_2O_3 *(N-8.1, F-7.3 at. %)*	4.9579(6)	13.6043(20)	22
N, F-co-doped Cr_2O_3 *(N-8.8, F-5.9 at. %)*	4.9597(4)	13.6055(15)	24

3.4.3 Morphology of the materials:

The FESEM image of as-prepared Cr_2O_3 shows that the particles have spherical morphology and are agglomerated (figure 3.7 (a)). The particle size is comparable to that obtained from X-ray diffraction data. On annealing, Cr_2O_3 nanoparticles undergo agglomeration to form bigger size particles as can be seen from FESEM image shown in figure 3.7(b).

FESEM images were taken for the N-doped, F-doped and N, F-co-doped samples (figure 3.7(c)-(e). The morphology of the samples is spherical and particle size is in the range of 20 nm – 30 nm, comparable to those obtained from XRD data.

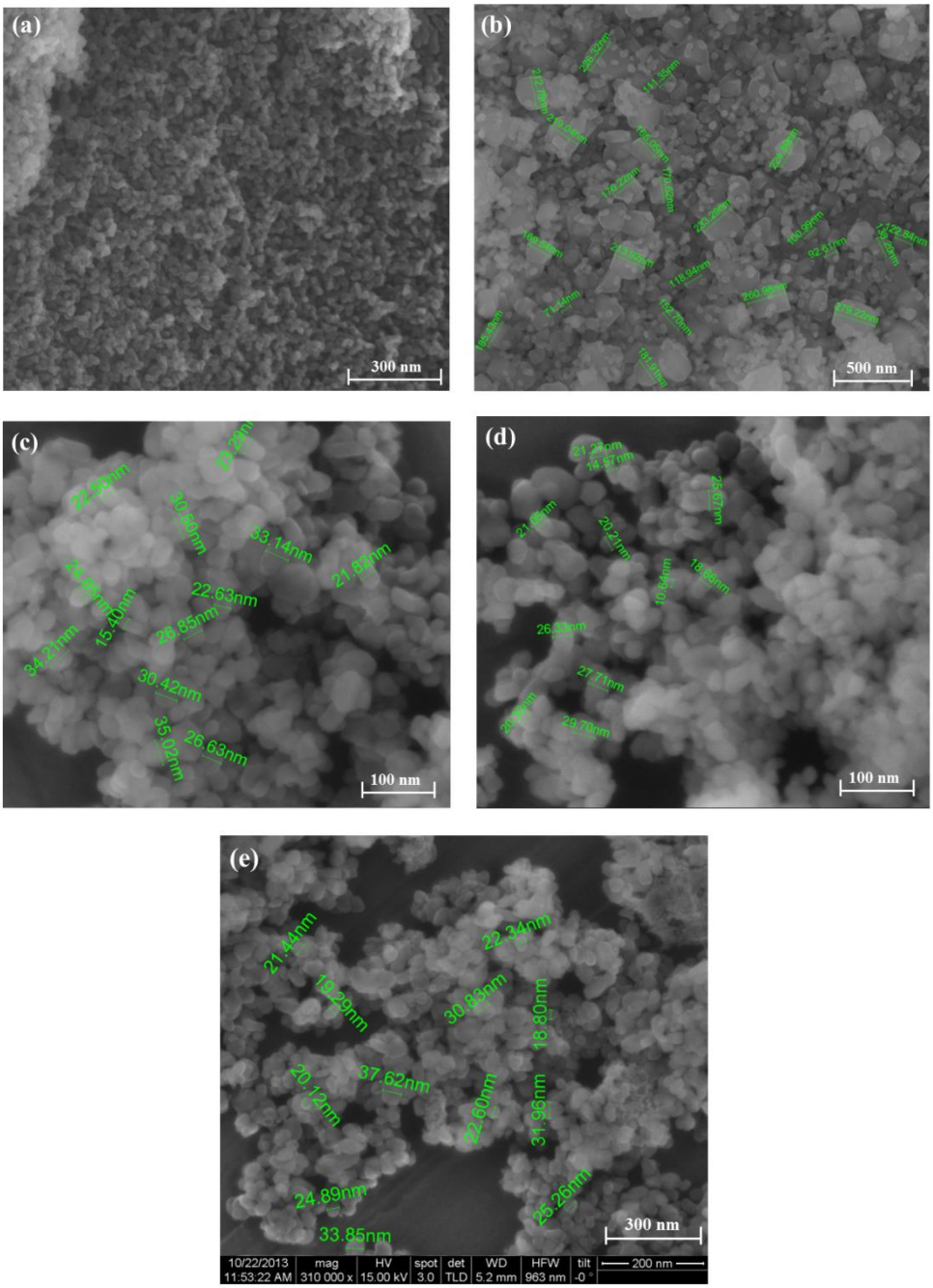

Fig 3.7 FESEM images of (a) Cr_2O_3 (before annealing) (b) Cr_2O_3 (after annealing) (c) F-doped Cr_2O_3 (F-11.2 at. %) (d) N-doped Cr_2O_3 (N-6.2 at. %) (e) N, F-co-doped Cr_2O_3 (N-8.8, F-5.9 at. %)

3.4.4 Magnetic Properties:

Cr_2O_3 is an antiferromagnet with the magnetic ordering temperature T_N = 308 K for bulk material. Figure 3.8 shows the field-cooled (FC) and zero-field cooled (ZFC) magnetization data in an applied magnetic field of 100 Oe and 1000 Oe for as-prepared Cr_2O_3 and annealed Cr_2O_3. The antiferromagnetic ordering temperature is clearly evident in case of annealed Cr_2O_3 (figure 3.8 (b)) and is similar to that of bulk. However, in case of as-prepared Cr_2O_3, FC magnetization in an applied field of 100 Oe shows that the antiferromagnetic ordering temperature is slightly shifted to 302 K (figure 3.8(a)). On applying a larger field (1000 Oe), T_N was found to be similar to that of bulk (figure 3.8(a) inset). This implies the presence of uncompensated spins on the surface of antiferromagnetic Cr_2O_3 nanoparticles. These uncompensated spins, at low temperature, tends to align along the field direction thereby increasing the magnetization at low temperature in case of as-prepared Cr_2O_3 (figure 3.8).

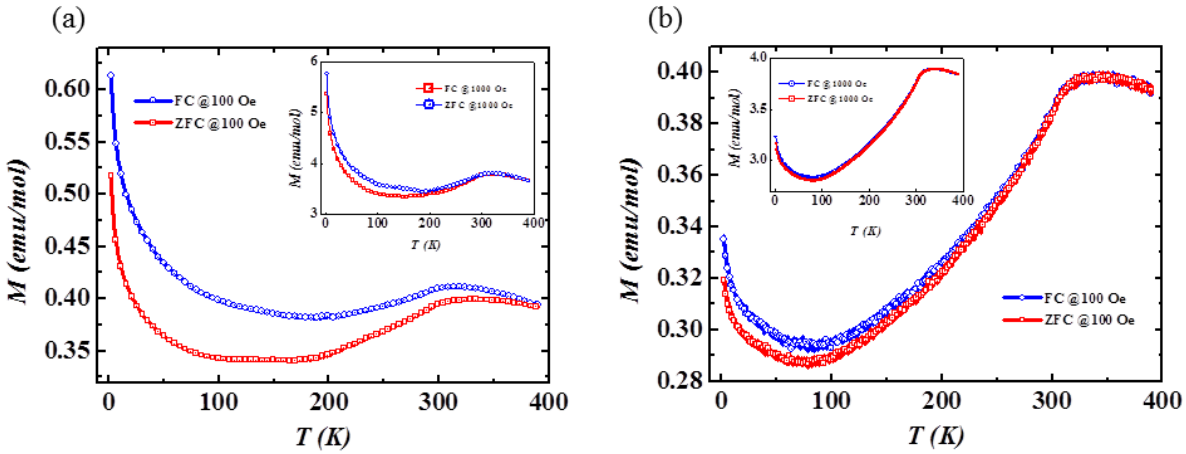

Fig 3.8 Variation of magnetization with temperature for (a) Cr_2O_3 (before annealing) (b) Cr_2O_3 (after annealing) under FC and ZFC conditions with H = 100 Oe and 1000 Oe (inset)

The ZFC magnetization of as-prepared Cr_2O_3 in an applied field of 100 Oe diverges from that of FC magnetization. This supports our inference that uncompensated spins are present on the surface of the nanoparticles. The observed divergence may be attributed to the alignment of the associated magnetic moments induced by cooling in presence of an external magnetic field. These moments were previously oriented in a

disordered fashion, but on cooling in presence of a field, tend to align along an easy axis closest to the direction of the field. On the other hand, cooling in the absence of a field does not drive the spin alignments along a particular direction while cooling. On increasing the applied field to 1000 Oe, there is a decrease in the divergence between FC and ZFC magnetization (figure 3.8(a) inset). This is as expected as large field forces the spins to align along the field direction irrespective of field-cooling or zero-field cooling.

Figure 3.9 shows the magnetization vs. magnetic field (*M-H*) curve for as-prepared Cr_2O_3 and annealed Cr_2O_3. *(M-H)* curve is linear in both the samples at temperature 2 K and 300 K. This shows the characteristic behaviour of an antiferromagnet.

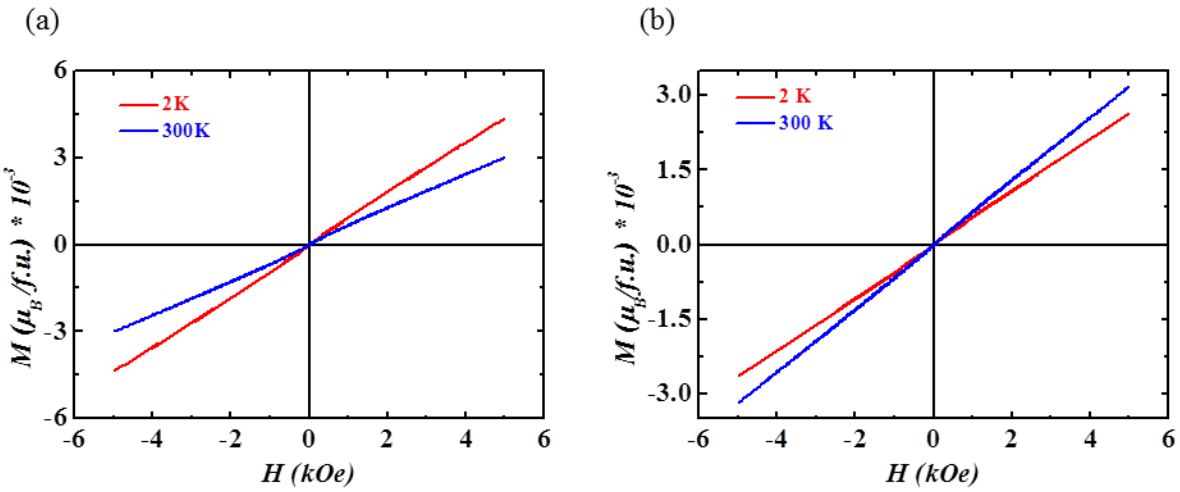

Fig 3.9 Variation of magnetization with applied magnetic field for (a) Cr_2O_3 (before annealing) (b) Cr_2O_3 (after annealing)

On doping Cr_2O_3 with fluorine, it was observed that the antiferromagnetic transition is less pronounced and is accompanied by a divergence in magnetization data measured under FC and ZFC conditions in an applied field of 100 Oe (figure 3.10(a)). As F is more electronegative than O, the 2p orbitals of F is lower in energy than that of O. As a result, F does not have any significant effect on the hybridization to form molecular orbitals. (*M-H)* curve of the F-doped sample was, however, found to be slightly non-linear as compared to that of undoped Cr_2O_3 (figure 3.10(b)).

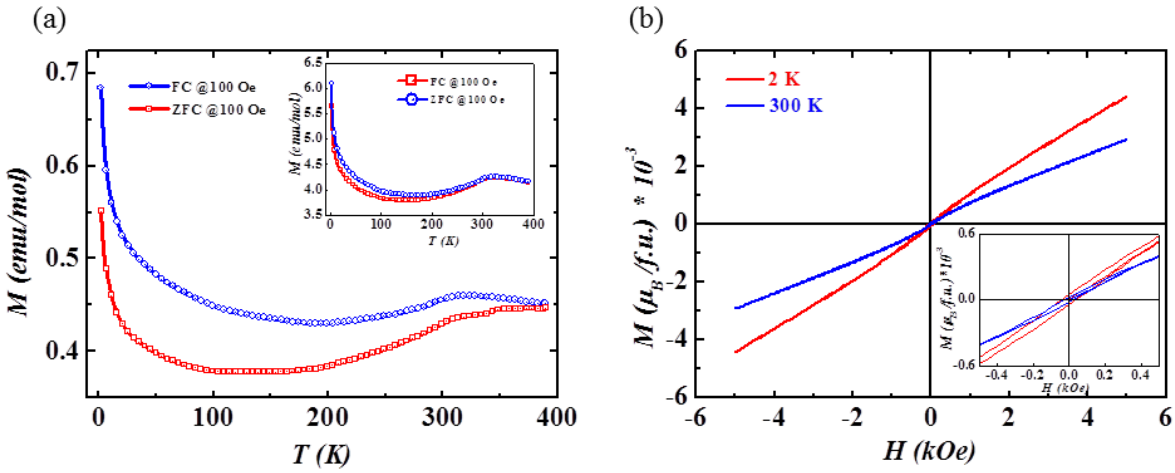

Fig 3.10 (a)M vs T curve under FC and ZFC conditions with an external magnetic field100 Oe (Inset H = 1000 Oe) (b) M vs H curve at temperature 2 K and 300 K for F-doped Cr_2O_3 (F-11.2 at. %)

Cr_2O_3, on doping with N, shows behaviour similar to that of F-doped Cr_2O_3. FC and ZFC magnetization curve in an applied field of 100 Oe shows divergence starting around the antiferromagnetic ordering temperature (figure 3.11). The divergence is more in case of N-doped Cr_2O_3 compared to that of undoped Cr_2O_3.

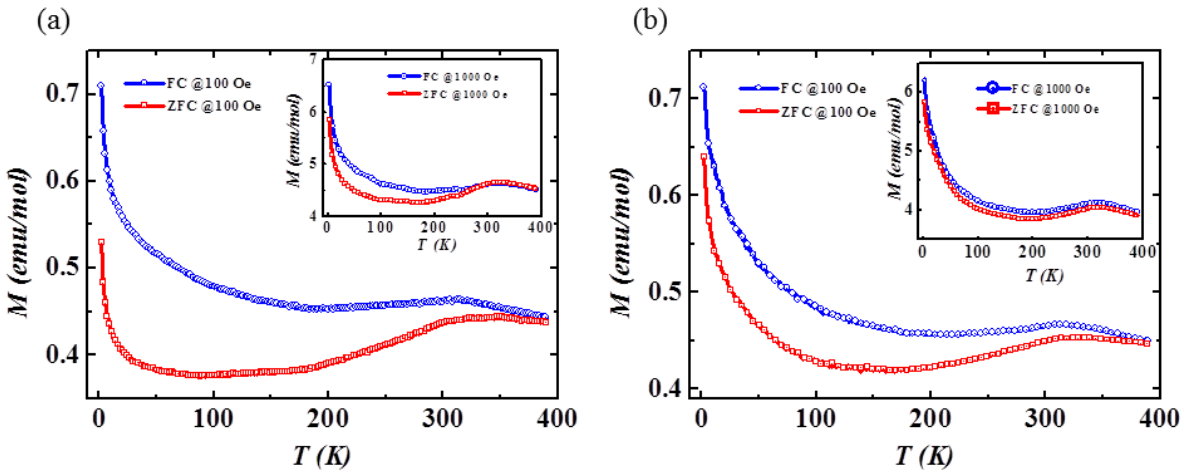

Fig 3.11 M vs T curve under FC and ZFC conditions with an external magnetic field 100 Oe (Inset H = 1000 Oe) for N-doped Cr_2O_3 (a) N-5.4 at. % (b) N-6.2 at. %

N-doped Cr_2O_3 shows a non-linear behaviour of magnetization as the applied field increase (figure 3.12).

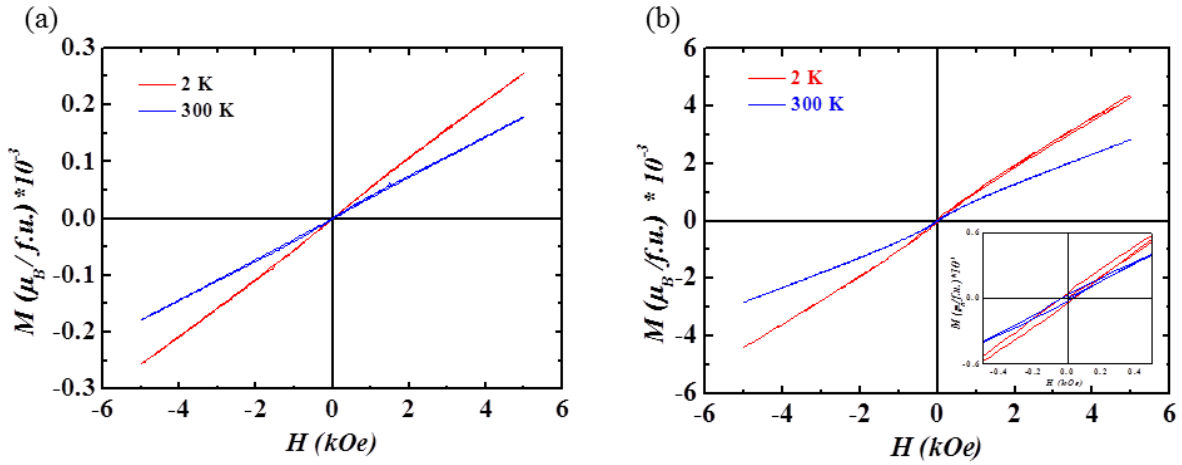

Fig 3.12 Variation of magnetization with applied magnetic field for N-doped Cr_2O_3 (a) N-5.4 at. % (b) N-6.2 at. %

. On co-doping Cr_2O_3 with N and F (5.1, 5.1 *at.* %), we continue to observe the divergence of FC and ZFC magnetization curve starting around T_N (figure 3.13(a)). Similar behaviour is observed for Cr_2O_3 co-doped with 8.1 *at.* % N and 7.3 *at.* % F.

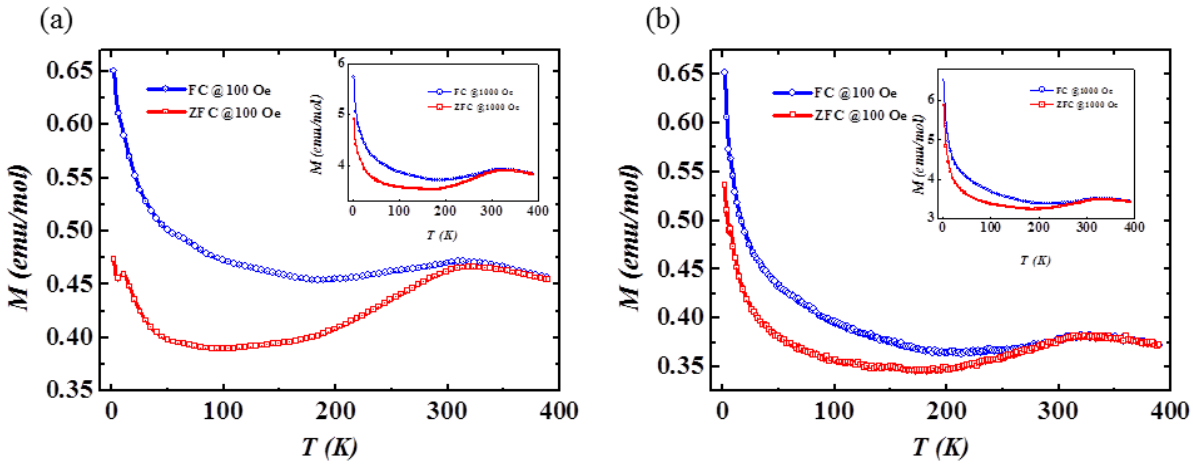

Fig 3.13 M vs T curve under FC and ZFC conditions with an external magnetic field 100 Oe (Inset H = 1000 Oe) for N, F-co-doped Cr_2O_3 (a) N-5.1, F-5.1 at. % (b) N-8.1, F-7.3 at. %

Moreover, magnetization increases with increase in applied field strength with slight non-linearity. *(M-H)* curve shows slight non-linearity. Similar behaviour was found with the sample doped with 8.1 *at.* % N and 7.3 *at.* % F.

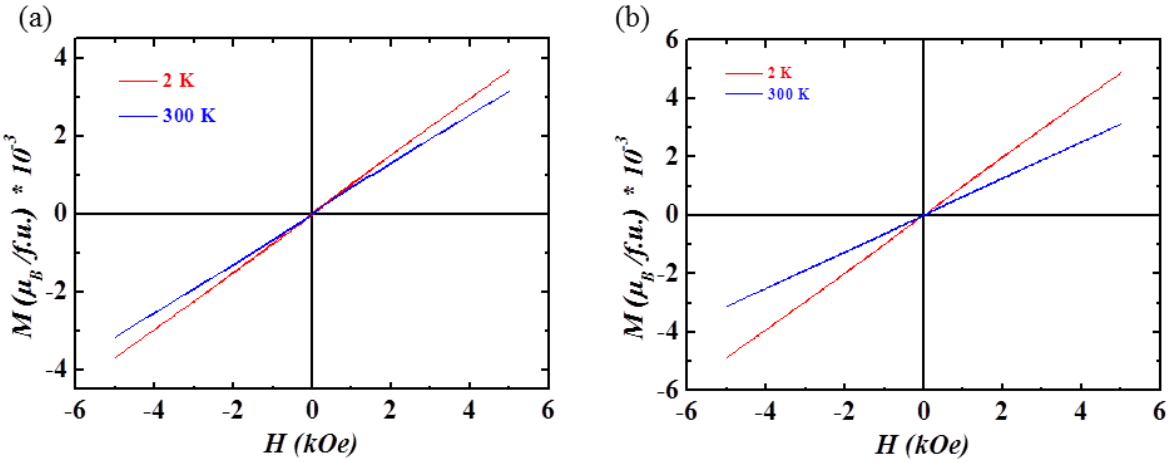

Fig 3.14 Variation of magnetization with applied magnetic field for N, F-co-doped Cr_2O_3 (a) N-5.1, F-5.1 at. % (b) N-8.1, F-7.3 at. %

However on co-doping Cr_2O_3 with different atomic percentage of nitrogen (8.8 at. %) and fluorine (5.9 at. %), a marked difference in the magnetic properties was observed. The particle size of all the samples studied (except the annealed Cr_2O_3) is in the range of 20 nm – 30 nm as was obtained from powder X-ray diffraction measurements and this range of particle size is complemented by FESEM images of those samples. This signifies that the particle size of this N, F co-doped Cr_2O_3 has no significant role in the observed behaviour. It is most likely the unequal proportions of N and F in the system that is responsible for such behaviour in this sample.

The magnetization of this N, F-co-doped sample is largely enhanced at low temperature, nearly doubled of the other samples at 2 K, at low magnetic field (100 Oe) as well as large magnetic field (1000 Oe) as shown in figure 3.15(a). Divergence of FC and ZFC magnetization at low field is much more prominent compared to that of undoped and other N and F doped samples. There is a huge drop in the ZFC magnetization with decrease in temperature. A strong irreversibility in the FC and ZFC magnetization curve signifies the presence of strong anisotropy in the system. Magnetic anisotropy tends to

align the magnetic moments in a preferred direction. As no magnetic field is applied while cooling the sample through T_N during the process of zero-field cooling, the magnetic moments are locked in random directions. On applying a small magnetic field at low temperature below T_N, the magnitude of the resultant magnetization depends on the anisotropy of the system. If the system is highly anisotropic, the small applied field is not sufficient to rotate the moments along the direction of the applied field and therefore ZFC magnetization is very small and a huge drop is observed at low temperature. During the FC magnetization measurement, the sample is cooled through T_N in the presence of an external magnetic field. As a result, the moments are probably locked in some particular direction closest to the direction of the applied field. If the system is highly anisotropic, the FC magnetization increases with decrease in temperature. This results to bifurcation of FC and ZFC curve.

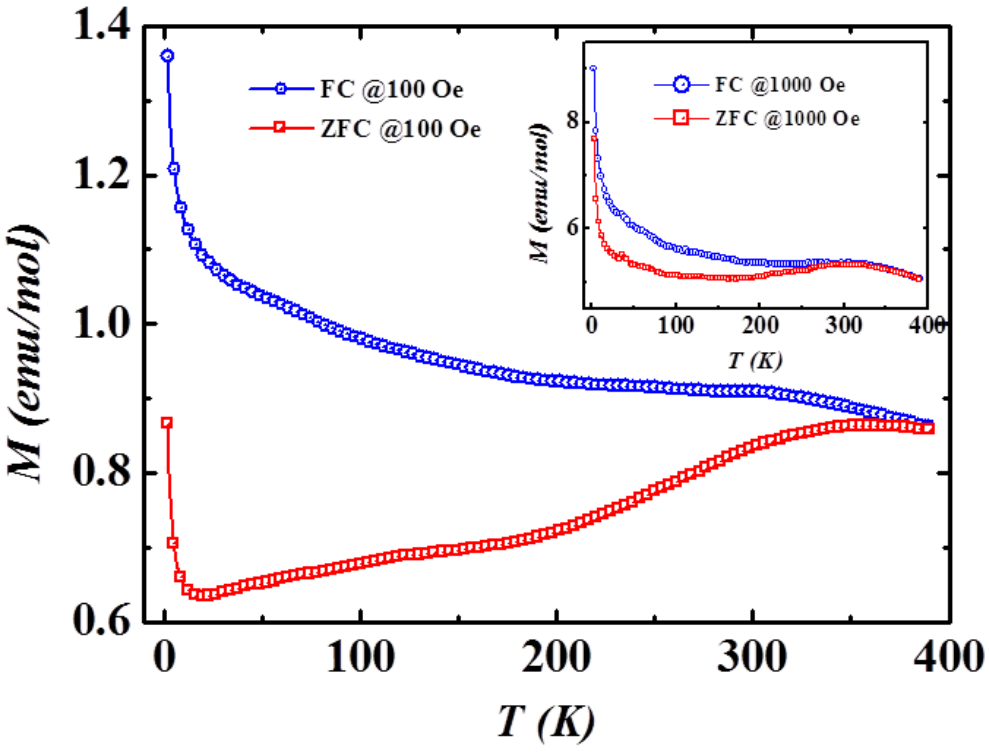

Fig 3.15 M vs T curve under FC and ZFC conditions with an external magnetic field100 Oe (Inset H = 1000 Oe) for N, F-doped Cr_2O_3 (N-8.8, F-5.9 at. %)

Moreover, the antiferromagnetic transition for this N, F-co-doped sample is no longer identifiable at low field (100 Oe). This may be attributed to large number of defects which is introduced in the system due to doping of N and F in unequal proportions. The defects in the system disturbed the antiferromagnetic ordering in the system and uncompensated spins must be present in the system besides the surface uncompensated spins that arises due to small particle size. This hypothesis is complemented by the observed huge divergence in FC and ZFC magnetization in this sample. We plotted the divergence of FC and ZFC magnetization with temperature for all the samples (figure 3.16) and we observe that divergence is most in this N, F- co-doped sample.

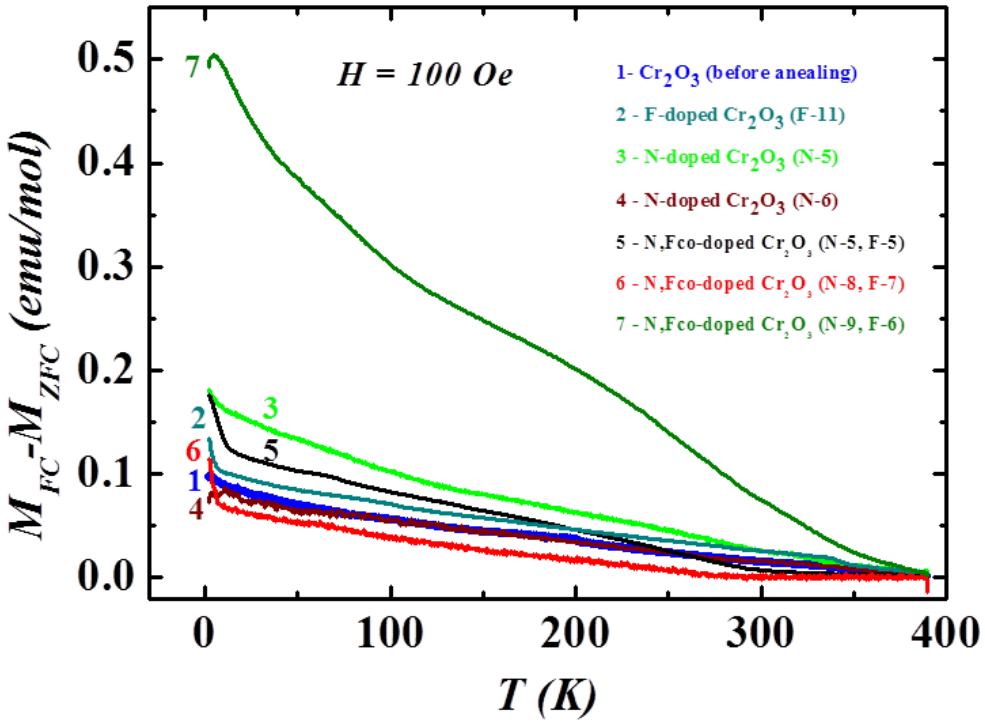

Fig 3.16 Variation of divergence of FC and ZFC magnetization in an applied field of 100 Oe with temperature for N, F-doped Cr_2O_3 (N-8.8, F-5.9 at. %)

There is a probability that the uncompensated spins present in the system experience short-ranged ferromagnetic ordering and co-exist with the antiferromagnetic

regions. It was indeed observed that this sample shows hysteresis behaviour of the magnetization without reaching the saturation regime (figure 3.17). The hysteresis behaviour persists even at 390 K but the coercitvity is not as prominent as it is in the case of 2 K temperature. (*M-H)* could not be measured beyond 390 K as the cold-pressed pellet of the sample was too brittle to be employed for higher temperature measurements. Moreover, annealing the pellet may result in alteration of N and F content of the sample. Presence of ferromagnetic CrO_2 is ruled out as the sample was synthesized at 600^{o}C while CrO_2 decomposes below 400^{o}C.

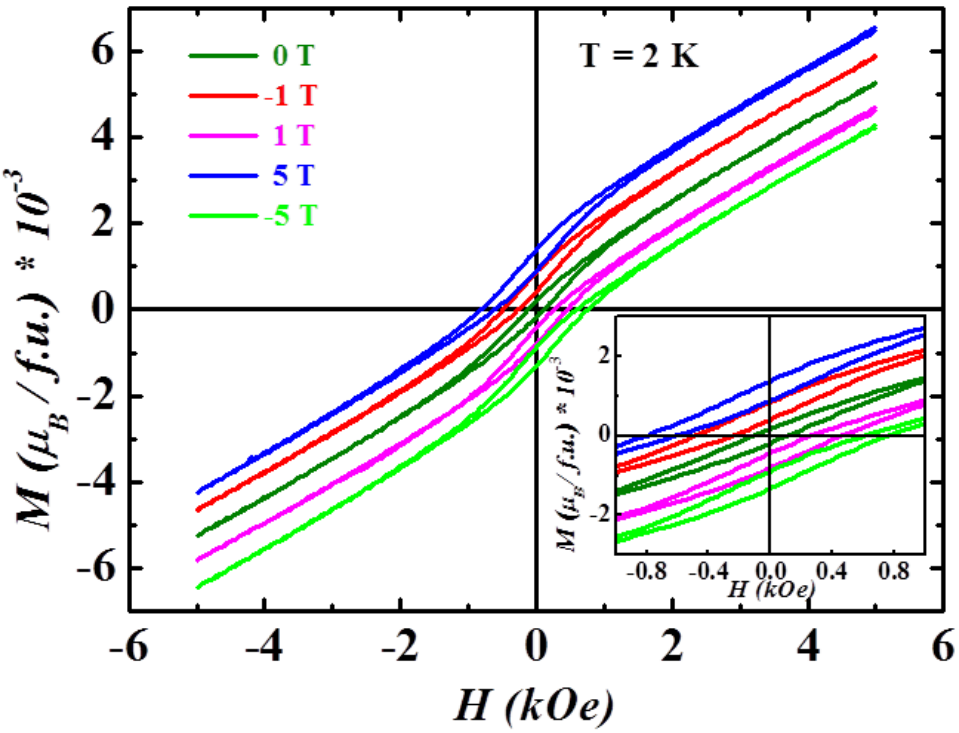

Fig 3.17 M-H curve for N, F-doped Cr_2O_3 (N-8.8, F-5.9 at. %) at 2 K at different cooling field

Variation in magnetization of this N, F-co-doped sample with varying magnetic field was studied by cooling the sample through T_N in the presence of different static DC magnetic field, *viz.* 1 T, 5 T, -1 T and -5 T. A systematic loop shift along the vertical axis was observed on cooling in presence of a field. The hysteresis loop shifts along the positive axis on cooling in positive field whereas it shifts along the negative axis on

cooling in presence of a negative field. The amount of loop shift increases with increase in cooling field strength (H_{FC}). Moreover, the coercivity of the hysteresis loop increases with increase in H_{FC}. It is much prominent in case of H_{FC} = 5 T and -5 T. However, we do not observe horizontal shift of the hysteresis loop. The remanence asymmetry M_E defined as $M_E = \frac{M_{R1}-M_{R2}}{2}$ and magnetic coercitivity M_C defined as $M_C = \frac{M_{R1}+M_{R2}}{2}$ where M_{R1} and M_{R2} are the top and bottom remanent magnetization of a hysteresis loop are calculated and are given in the table 3.2. The exchange bias field H_E defined as $H_E = \frac{H_{C1}+H_{C2}}{2}$ and the coercive field H_C defined as $H_C = \frac{H_{C1}-H_{C2}}{2}$ where H_{C1} and H_{C2} are left and right coercive field are also given in the table 3.2.

Table 3.2 M_E, M_C, H_E and H_C values of 8.8 a.t % N and 5.9 at. % F-co-doped Cr_2O_3

H_{FC}	M_{R1} (μ_B/f.u.) $\times 10^{-4}$	M_{R2} (μ_B/f.u.) $\times 10^{-4}$	M_C (μ_B/f.u.) $\times 10^{-4}$	M_E (μ_B/f.u.) $\times 10^{-4}$	H_{C1} (Oe)	H_{C2} (Oe)	H_C (Oe)	H_E (Oe)
-5 T	13.83	8.89	2.47	11.36	-137	136	-136.5	-0.5
-1 T	8.57	4.07	2.25	6.32	-126	125	-125.5	-0.5
0 T	1.83	-1.83	0.83	0.00	-112	111	-111.5	0.5
1 T	-4.32	-8.08	1.88	-6.20	-108	104	-106	-2
5 T	-8.83	-13.24	2.20	-11.03	-120	122	-121	-1

It is clear that the exchange bias field H_E is almost zero irrespective of the cooling field. However, the coercive field H_C increases by 20 Oe when H_{FC} = 5 T compared to that of zero-field cooling.

The shift in hysteresis loop was studied at different temperatures for after cooling in presence of field H_{FC} = 1 T. The hysteresis loop moves towards the origin on increasing the temperature from 2 K to 350 K. At 300 K, the centre of gravity of the loop becomes the origin. It is shown as M_E *vs.* T plot in figure 3.18. M_E becomes almost zero at T = 300 K.

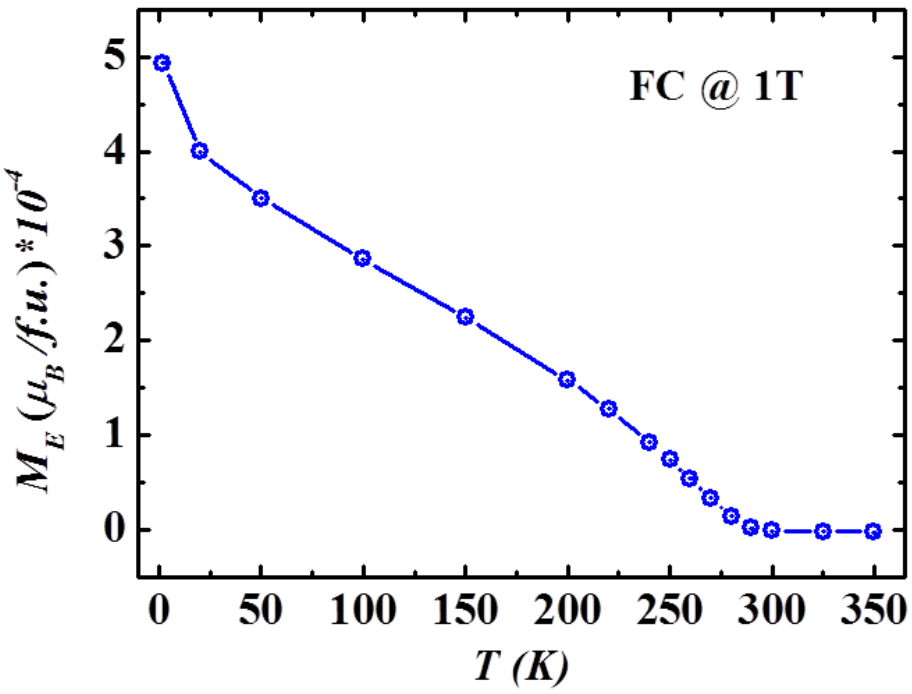

Fig 3.18 M_E vs. T plot for N, F-doped Cr_2O_3 (N-8.8, F-5.9 at. %) for H_{FC} = 1 T

One probable explanation for the observed behaviour of this N, F-co-doped Cr2O3 is that the uncompensated spins which are present in the system behave like spin-glass system and are locked in a preferred orientation while cooling in presence of an external magnetic field. The spin-glass system and the antiferromagnetic core behaves like an exchange bias system resulting to an exchange bias effect[12]. To understand the underlying phenomenon of the observed behaviour, AC magnetization of the sample was measured. However, we fail to observe any characteristic behaviour of spin-glass like system. Moreover, H_E is close to zero irrespective of the strength of cooling field which signifies that there is no exchange bias effect in the system.

However as there is vertical shift of the hysteresis loop and also slight increase in the coercivity with increase in the strength of cooling field, we expect that the uncompensated spins are pinned by the antiferromagnetic core. We need to further investigate to understand the system thoroughly.

We made an attempt to fit inverse molar susceptibility χ_M *vs.* temperature T plot. But the linear region is too small to get a reliable quantitative value and due to the limitation of the sample discussed above, the magnetization data cannot be obtained beyond 390 K. Therefore, relatively speaking, Curie-Weiss constant θ_{CW} of pure Cr_2O_3 is highly negative. However, the magnitude of θ_{CW} decreases on doping with N and co-doping with N and F and lowest value is found in the 8.8 *at*. % N and 5.9 *at.* % F co-doped Cr_2O_3 sample where hysteresis loop was observed. This implies that some ferromagnetic interaction is likely to be present in the system.

Table 3.3 Curie-Weiss constant for undoped and N, F doped and co-doped Cr_2O_3

Sample	θ_{CW} *(K)*
Cr_2O_3	-2079
5.4 *(6.2)* at % N-doped Cr_2O_3	-1156 *(-1302)*
11.2 at % F-doped Cr_2O_3	-2414
5.1 *(8.1)* at % N, 5.1 *(7.3)* at % F-co- doped Cr_2O_3	-1305 *(-1483)*
8.8 at % N, 5.9 at % F-co-doped Cr_2O_3	-896

3.4.5 Optical Properties:

Figure 3.19 shows the Raman spectra of undoped Cr_2O_3 and N and F doped and co-doped Cr_2O_3. Raman peaks are observed at 303 cm^{-1}, 344 cm^{-1}, 544 cm^{-1}, 601 cm^{-1} in all the samples. The peak at 544 cm^{-1} is due to a vibrational mode of A_{1g} symmetry and the other observed peaks are due to vibrational mode of E_g symmetry[13]. No change in Raman spectra is observed on doping with N or F or both.

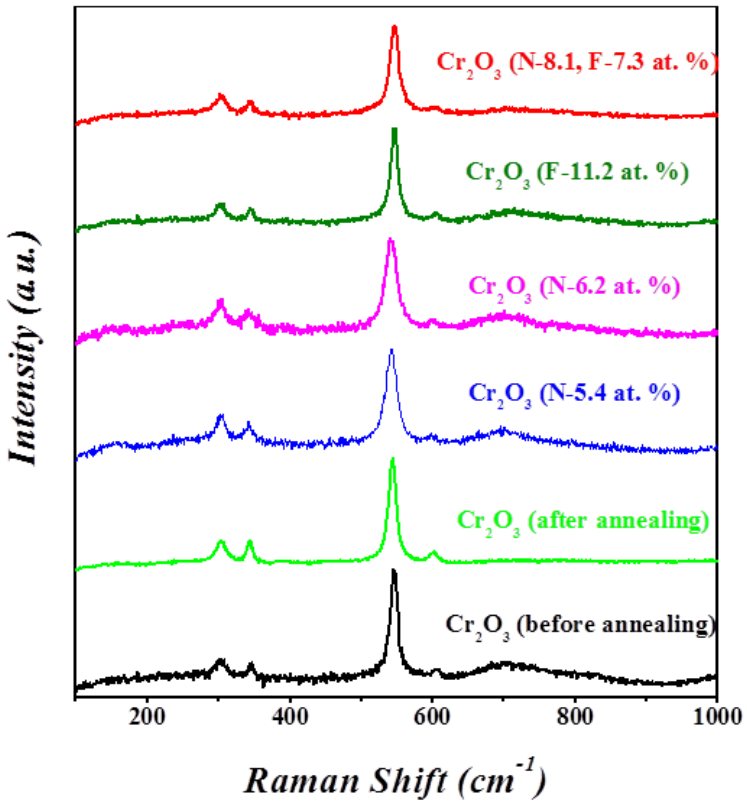

Figure 3.19 Raman spectra of undoped Cr_2O_3 and N and F doped and co-doped Cr_2O_3

UV-visible absorption spectroscopy was also studied for these samples (figure 3.20). Two absorption bands were observed viz. one from 410 nm to 540 nm and the other from 540 nm to 800 nm. The first absorption band corresponds to $^4A_{2g}$ to $^4T_{1g}$ transition and the second absorption band corresponds to $^4A_{2g}$ to $^4T_{2g}$ transition. On doping with F, a slight shift in the absorption bands is observed. On doping with N and co-doping with N and F, we see a definite increase in λ_{max} of both the transitions. In case of 8.8 *at.* % N and 5.9 *at.* % F co-doped Cr_2O_3, the absorption bands appear at 462.7 nm and 601.5 nm compared to 461 nm and 599 nm of Cr_2O_3. As expected, there is a small yet significant red shift. Table 3.4 shows the peak positions of the two transitions for the doped and undoped samples.

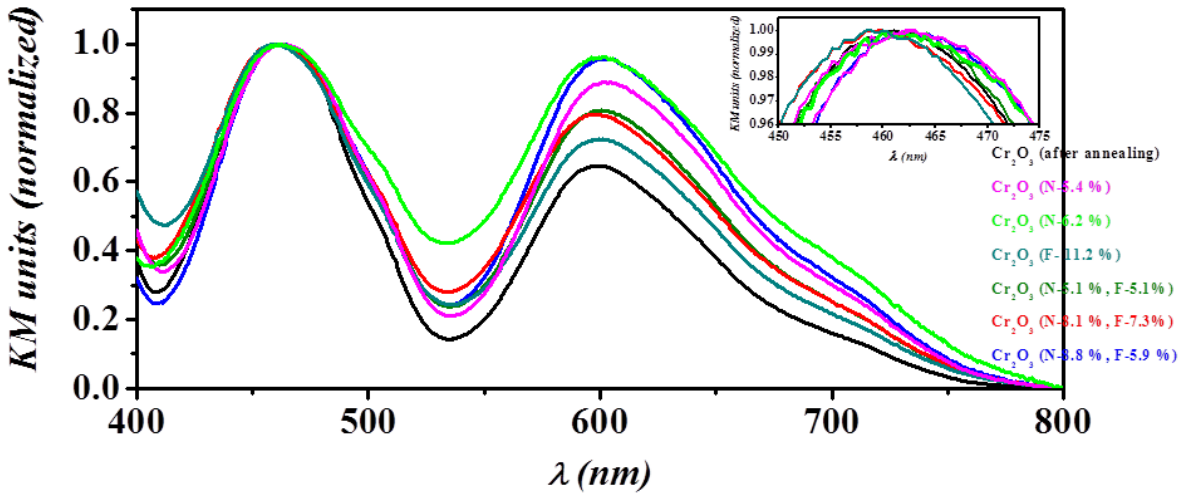

Figure 3.20 UV-visible absorption spectra of undoped Cr_2O_3 and N and F doped and co-doped Cr_2O_3

Table 3.4 UV-visible absorption bands for undoped and N, F doped and co-doped Cr_2O_3

Sample	λ (nm)	
	$^4A_{2g} \longrightarrow {}^4T_{1g}$	$^4A_{2g} \longrightarrow {}^4T_{2g}$
Cr_2O_3	461	599
5.4 *(6.2)* at % N-doped Cr_2O_3	461.6 *(462.6)*	602.5 *(599.9)*
11.2 at % F-doped Cr_2O_3	459.4	600
5.1 *(8.1)* at % N, 5.1 *(7.3)* at % F-co- doped Cr_2O_3	461.5 *(459)*	600.7 *(598.4)*
8.8 at % N, 5.9 at % F-co-doped Cr_2O_3	462.7	601.5

3.5 Conclusion:

We have substituted oxygen in Cr_2O_3 with different concentration of nitrogen and fluorine. We have obtained up to 6.2 *at.* % of N content in N-doped sample and up to 11.2 *at.* % of F content in F-doped sample. We have carried out co-doping of Cr_2O_3 with N

and F as well. We could obtained equal proportion of N and F in one sample and in another, the concentration of N was 1.5 times more than that of F. This particular N, F-co-doped sample presents unique and interesting properties due to the defects introduced in the system. It shows a huge divergence in the FC and ZFC magnetization curves. The antiferromagnetic transition was not clearly identifiable. Moreover, a weak ferromagnetism was observed and the hysteresis loop shifts along the vertical axis on cooling in presence of an external field. A slight increase in the coercive field on increasing H_{FC} was also observed.

Anion doping of Cr_2O_3 therefore opens up a new dimension in the research of magnetoelectric materials.

3.6 References:

[1] (a) I. S. Elfimov, A. Rusydi, S. I. Csiszar, Z. Hu, H. H. Hsieh, H. J. Lin, C. T. Chen, R. Liang, G. A. Sawatzky, *Phys. Rev. Lett.* **2007**, *98*, 137202; (b) R. Asahi, T. Morikawa, T. Ohwaki, K. Aoki, Y. Taga, *Science* **2001**, *293*, 269-271.

[2] T. Shiroka, G. Lamura, S. Sanna, G. Prando, R. De Renzi, M. Tropeano, M. R. Cimberle, A. Martinelli, C. Bernini, A. Palenzona, R. Fittipaldi, A. Vecchione, P. Carretta, A. S. Siri, C. Ferdeghini, M. Putti, *Phys. Rev. B* **2011**, *84*, 195123.

[3] (a) K. Nitesh, P. Jaysree, N. Aysha, V. W. Umesh, A. Sundaresan, C. N. R. Rao, *J. Phys.: Condens. Mat.* **2013**, *25*, 345901; (b) R. Saha, S. Revoju, V. I. Hegde, U. V. Waghmare, A. Sundaresan, C. N. R. Rao, *ChemPhysChem* **2013**, *14*, 2672-2677.

[4] N. Kumar, U. Maitra, V. I. Hegde, U. V. Waghmare, A. Sundaresan, C. N. R. Rao, *Inorg. Chem.* **2013**, *52*, 10512-10519.

[5] S. Foner, *Phys. Rev.* **1963**, *130*, 183-197.

[6] K. Yohei, I. Hiroshi, S. Munetaka, *Appl. Phys. Express* **2013**, *6*, 113007.

[7] M. Muto, Y. Tanabe, T. Iizuka-Sakano, E. Hanamura, *Phys. Rev. B* **1998**, *57*, 9586-9607.

[8] O. Nishimura, K. Yabe, M. Iwaki, *J. Electron Spectrosc.* **1989**, *49*, 335-342.

[9] F. P. Larkins, A. Lubenfeld, *J. Electron Spectrosc.* **1979**, *15*, 137-144.

[10] D. N. Hendrickson, J. M. Hollander, W. L. Jolly, *Inorg. Chem.* **1969**, *8*, 2642-2647.

[11] E. Kemnitz, A. Kohne, I. Grohmann, A. Lippitz, W. E. S. Unger, *J. Catal.* **1996**, *159*, 270-279.

[12] E. C. Passamani, C. Larica, C. Marques, A. Y. Takeuchi, J. R. Proveti, E. Favre-Nicolin, *J. Magn. Magn. Mater.* **2007**, *314*, 21-29.

[13] J. Mougin, T. Le Bihan, G. Lucazeau, *J. Phys. Chem. Solids* **2001**, *62*, 553-563.